Relic density and direct detection rate of neutralino dark matter in the MSSM

T. Nihei (Nihon Univ.)

Feb. 6, 2004 at KEK

in collaboration with

Y.G. Kim, L. Roszkowski (Lancaster U.),
R. Ruiz de Austri (Thessaloniki U.)

References

Kim–T.N.–Roszkowski–Ruiz de Austri, JHEP0212 (2002).
T.N.–Roszkowski–Ruiz de Austri, JHEP0207 (2002);
JHEP0203 (2002); JHEP0105 (2001).
Roszkowski–Ruiz de Austri–T.N., JHEP 0108 (2001).

Contents

I. Introduction

Cosmological observations

■ Relic density

New CMB observations (Boomerang, MAXIMA, $\cdots$)

$\searrow\ 0.1 < \Omega_\chi h^2 < 0.3$

WMAP (2001–, NASA)

$\Omega_m h^2 = 0.135^{+0.008}_{-0.009}$, $\Omega_b h^2 = 0.0224 \pm 0.0009$

$\Omega_\nu h^2 < 0.0067$

$\Omega_i \equiv \rho_i/\rho_c$

$h \approx 0.7$

$\longrightarrow$ Relic density of cold dark matter

$H_0 = 100h$ km/s/Mpc

$\Omega_\chi h^2 = 0.1126^{+0.016}_{-0.018}$ (χ: CDM)

WMAP, Planck (2007–) —— $\Omega_\chi h^2$ with $\lesssim$ 10 % accuracy

■ Direct detection

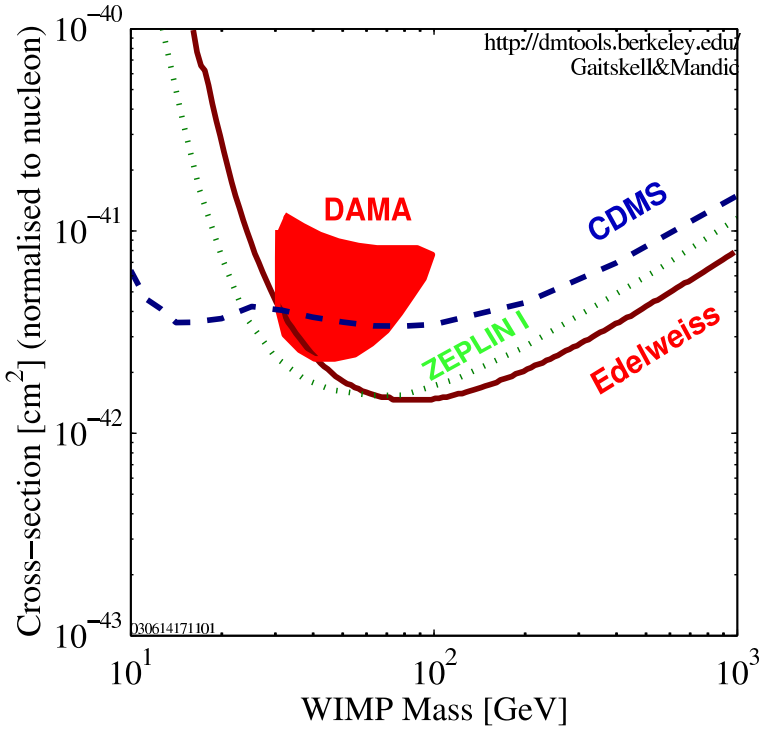

Weakly Interacting Massive Particle (WIMP)

$\chi p \to \chi p$

- DAMA (NaI)
- CDMS (Ge & Si)
- ZEPLIN (Xe)
- Edelweiss (Ge)
- ⋮

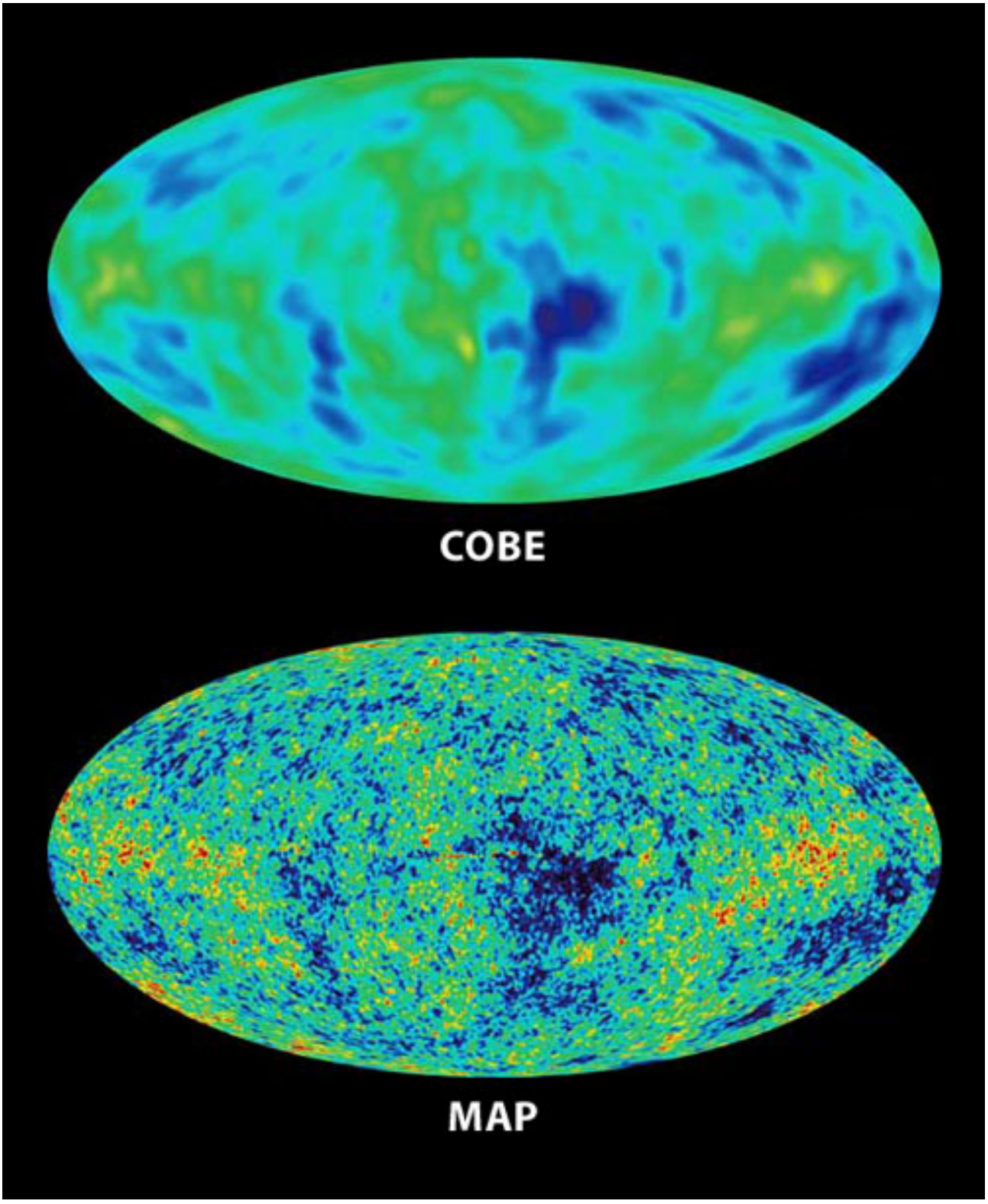
COBE
MAP

Table 1: Decomposition of the rate equation (1).

Particle-Physics	Astro-Physics	Detector-Physics
m_w	$n_0 = \rho_0/m_w$	$\mathrm{F}^2(Q)$
σ_0	f(v)	m_n
	v_{max}	N_T
		E_R
unknown	estimates	minor uncertainty

Ramachers
astro-ph/0211500

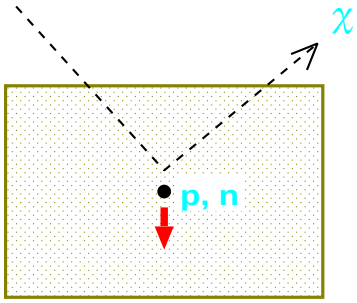

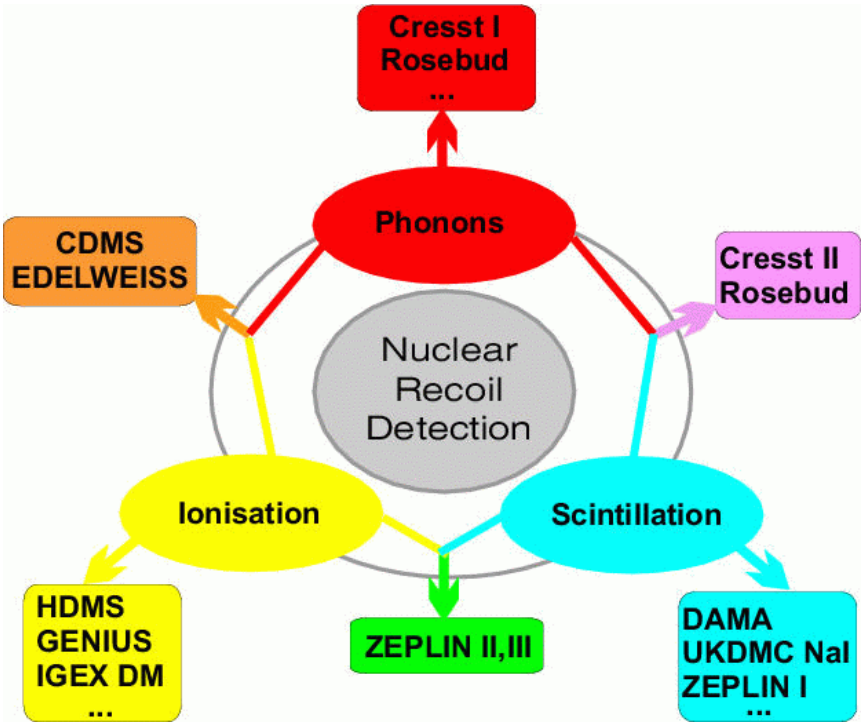

Figure 2: Classification scheme for WIMP direct detection techniques.

the WIMP dark halo of our galaxy. The escape velocity, v_{max}, determines the cutoff of the WIMP energy spectrum at high energies, typically below 100 keV, since its value being around 600 km/s. A more important parameter is the local halo density, ρ_0, since the WIMP signal is directly proportional to its value. This particular number represents rather an assumption than a reasonable guess. It is very uncertain, to a factor two or even more, since its value is strongly linked to the assumed halo model. The precise dark halo model would determine also the WIMP velocity distribution, f(v). However, since any dark halo model is so far merely an assumption, both, the WIMP halo density and the WIMP velocity distribution represent a significant systematic uncertainty. The determination of a dark halo model is currently a very active topic of research in astrophysics ([11] and references therein). Meanwhile, the WIMP direct detection community uses a canonically assumed halo model, the simplest reasonable model fixing the density at a value of 0.3 GeV/cm^3 and

Supersymmetry (SUSY)

Λ: cutoff

- Naturalness

$$m_{\rm Higgs}^2 = m_0^2 + \quad + \quad$$

$$= m_0^2 + \alpha\Lambda^2 - \alpha\Lambda^2$$

Quadratic divergence cancelled

exact SUSY $\longrightarrow m_{\tilde{e}} = m_e\,, \cdots$

superpartners: not discovered yet

$\longrightarrow$ soft SUSY breaking ($\widetilde{m}$)

$$\begin{cases} \text{superpartner: heavy} \\ \Lambda^2 \text{ cancellation: kept} \end{cases}$$

$\longrightarrow \widetilde{m} = 100$ GeV – a few TeV

$$m_{\rm Higgs}^2 = m_0^2 + \alpha\widetilde{m}^2$$

- Gauge coupling unification

Non SUSY SUSY $\alpha_i = g_i^2/4\pi$

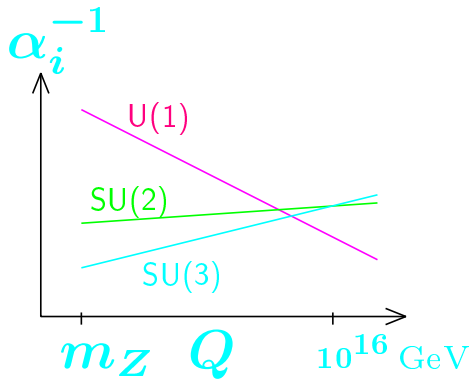

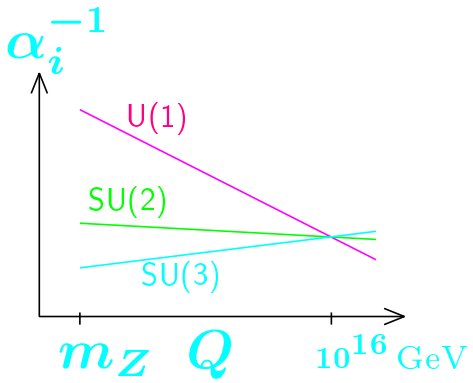

■ Minimal supersymmetric SM (MSSM)

- Particle contents:

spin $= 0$	$1/2$	1
$\widetilde{q}\ \ \widetilde{u}\ \ \widetilde{d}$	$q\ \ u\ \ d$	
$\widetilde{\ell}\ \ \widetilde{e}$	$\ell\ \ e$	
$H_1\ \ H_2$	$\widetilde{H}_1\ \ \widetilde{H}_2$	
	$\widetilde{B}\ \ \widetilde{W}^a\ \ \widetilde{g}^\alpha$	$B_\mu\ \ W_\mu^a\ \ g_\mu^\alpha$

Higgses $h^0,\ H^0,\ A^0,\ H^\pm$ ⟵ $H_1\ \ H_2$

-ino mass eigenstates

$$\begin{cases} \widetilde{H}_1^-, \widetilde{H}_2^+, \widetilde{W}^1, \widetilde{W}^2 \longrightarrow \text{charginos} & \chi_{1,2}^\pm \\ \widetilde{H}_1^0, \widetilde{H}_2^0, \widetilde{B}, \widetilde{W}^3 \longrightarrow \text{neutralinos} & \chi_{1,2,3,4}^0 \end{cases}$$

R-parity ⟶ Lightest Super Particle (LSP): stable

⟶ DM candidate ($\chi = \chi_1^0$)

- Relevant terms:

gaugino mass $\frac{1}{2}(M_1\widetilde{B}\widetilde{B} + M_2\widetilde{W}^a\widetilde{W}^a + M_3\widetilde{g}^\alpha\widetilde{g}^\alpha)$

Higgisno mass $\mu\widetilde{H}_1\widetilde{H}_2 + \text{h.c.}$

Higgs mass $\mu^2(|H_1|^2 + |H_2|^2) + \cdots$

$\longrightarrow \tan\beta = \langle H_2^0\rangle/\langle H_1^0\rangle,\ m_A^2|A|^2$

sfermion mass $m_{\widetilde{q}_i}^2|\widetilde{q}_i|^2 + m_{\widetilde{\ell}_i}^2|\widetilde{\ell}_i|^2 + \cdots$

(+ scalar trilinear couplings $A_t\widetilde{t}_R^\dagger\widetilde{q}_L H_2 + \cdots$)

[cf. Constrained MSSM (CMSSM)
$m_0,\ m_{1/2},\ A_0,\ \tan\beta,\ \text{sgn}(\mu)$]

■ R–parity

$$R = \begin{cases} +1 & \text{SM particles} \\ -1 & \text{superpartners} \end{cases}$$

Without R–parity $\longrightarrow$ Rapid proton decay via dim 4 op.

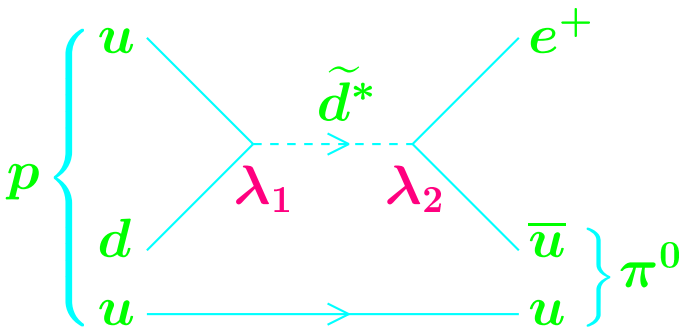

λ_1, λ_2 (dim=0) $\longrightarrow$ unnaturally small

R–parity $\longrightarrow$ LSP is stable

$$\begin{cases} \bullet & \text{SM particles} \\ \circ & \text{superpartners} \end{cases}$$

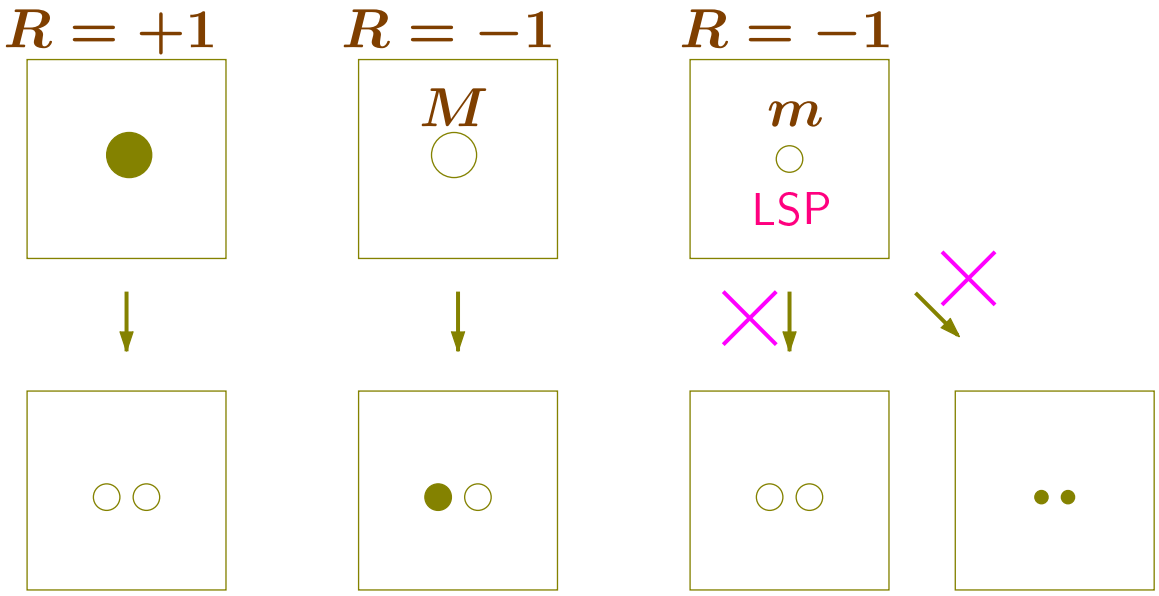

■ Constrained MSSM (CMSSM)

- Soft ~~SUSY~~ parameters at $Q = M_{\rm GUT}$ $(\approx 2 \times 10^{16}\,{\rm GeV})$

  scalars $\quad m^2_{\tilde{q}_i} = m^2_{\tilde{\ell}_i} = m^2_{H_1} = m^2_{H_2} = m_0^2$

  gauginos $\quad M_1 = M_2 = M_3 = m_{1/2}$

  trilinear $\quad A_{U,D,E} = A_0 Y_{U,D,E}$

- RGE: $M_{\rm GUT} \longrightarrow m_Z$

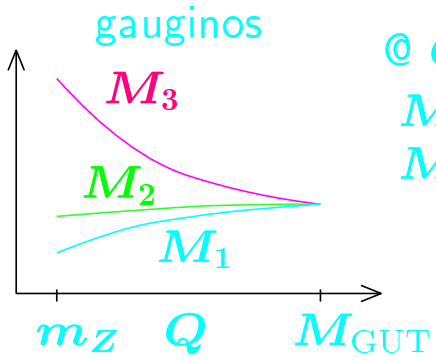

@ $Q = m_Z$

$M_1 \approx M_2/2$

$M_3 \approx 3M_2$

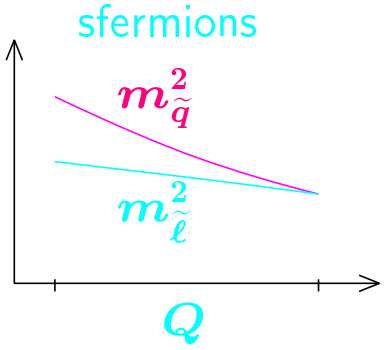

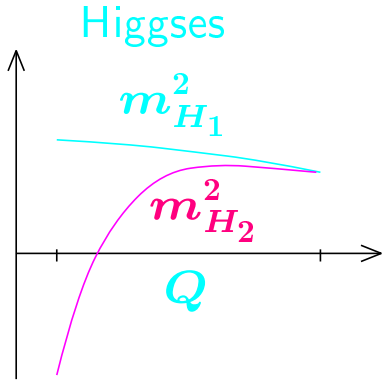

Radiative EW symmetry breaking (EWSB)

$m^2_{\rm Higgs} = m_0^2 > 0$ at $M_{\rm GUT}$

$\longrightarrow m^2_{\rm Higgs} < 0$ at m_Z

$$\left[\frac{m_Z^2}{2} = \frac{m^2_{H_1} - m^2_{H_2}\tan^2\beta}{\tan^2\beta - 1} - \mu^2\right]$$

$\Downarrow$

$4 + 1$ parameters

$m_0,\ m_{1/2},\ A_0,\ \tan\beta,\ {\rm sgn}(\mu)$

Experimental constraints

LEP

- Chargino mass bound: $m_{\chi_1^\pm} > 104\,\mathrm{GeV}$
- Lightest Higgs mass bound: $m_h > 114\,\mathrm{GeV}$ (SM)

  $\longrightarrow$ conservative bound: $m_h > 111\,\mathrm{GeV}$

m_A dep.
$m_h > 0.78\,(m_A + 21.7\,\mathrm{GeV})$
for $m_A < 120\,\mathrm{GeV}$

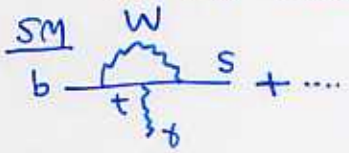

$b \to s\gamma$

CLEO, BELLE

$$\mathrm{Br}(B \to X_s\gamma)_{\mathrm{EXP}} = (3.41 \pm 0.36) \times 10^{-4}$$

SM prediction: consistent with exp.

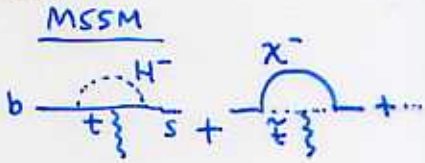

$\longrightarrow$ conservative bound

$$\mathrm{Br}(B \to X_s\gamma) = (3.41 \pm 0.67) \times 10^{-4}$$

Muon $g-2$

E821 experiment (e^+e^- annihilation data) $\qquad a_\mu \equiv (g_\mu - 2)/2$

$$a_\mu^{\mathrm{exp}} - a_\mu^{\mathrm{SM}} = (33.9 \pm 11.2) \times 10^{-10}$$

3 σ discrepancy

$$11.5 \times 10^{-10} < a_\mu^{\mathrm{SUSY}} < 56.3 \times 10^{-10} \quad (2\sigma)$$

MSSM

$$\left[\ 22.7 \times 10^{-10} < a_\mu^{\mathrm{SUSY}} < 45.1 \times 10^{-10}\ (1\sigma)\ \right]$$

preferred region

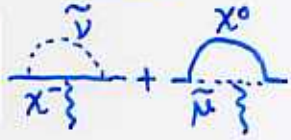

Which is the LSP?

Ellis etal
NP B238 ('84)

$$\text{MSSM} \sim \begin{pmatrix} q, \ell, \nu ; & W, Z, \gamma, g ; & H \\ \tilde{q}, \tilde{\ell}, \tilde{\nu} ; & \tilde{g}, \chi^0, \chi^\pm & \end{pmatrix}$$

$\chi^\pm$ or $\tilde{\ell}^\pm$

$$n_{LSP} \sim 10^{-6} \left(\frac{m_{LSP}}{GeV}\right) n_B$$

→ anomalously heavy proton searches
(null results)

$\tilde{q}$ or $\tilde{g}$

bound states

- charged → anomalously heavy p
- neutral → possible (but not in mSUGRA)

$\tilde{\nu}$

ruled out by WIMP direct detection

(Usually slightly light $\tilde{\ell}$'s exist)

χ^0

χ_1^0 = LSP : most likely

II. Relic density

■ Calculation of relic density

Boltzmann eq.

$$\frac{dn_\chi}{dt} + 3Hn_\chi = -\langle \sigma v_{\rm rel}\rangle (n_\chi^2 - n_\chi^{\rm eq2})$$

Accurate calculation

1. All the contributions to $\sigma = \sigma(\chi\chi \to \text{all})$ NRR (2001)

   "all" $= f\bar{f}$, W^+W^-, ZZ, hh, hH, HH, HA, AA, H^+H^-, Zh, ZH, ZA, $W^\pm H^\mp$

2. Exact formula for $\langle \sigma v\rangle$ Gondolo–Germini (1991)

   $\longleftrightarrow$ expansion $\langle \sigma v\rangle = a + bx$, $x = T/m_\chi$

3. Accurate treatment of Boltzmann eq.

   $\longleftrightarrow$ approximate solution

   $$\rho_\chi \propto 1/\int_0^{x_f} dx \langle \sigma v\rangle, \quad x_f = T_f/m_\chi \sim 1/20$$

4. Coannihilation ($\chi\chi' \to \cdots$, $\chi'\chi' \to \cdots$, $\cdots$) Griest–Seckel (1991)

   Mizuta–Yamaguchi (1993)

   χ': NLSP ($\widetilde{\tau}_1$, $\chi_1^\pm$, χ_2^0, $\cdots$)

   important for $m_{\chi'} \lesssim 1.1 m_\chi$

   $\sigma \longrightarrow \sigma_{\rm eff}$ enhanced

In our code, $\Omega_\chi h^2$ can be computed reliably.

- $\widetilde{H}$–like LSP
- resonance
- coannihilation

$\longrightarrow$ small $\Omega_\chi h^2$

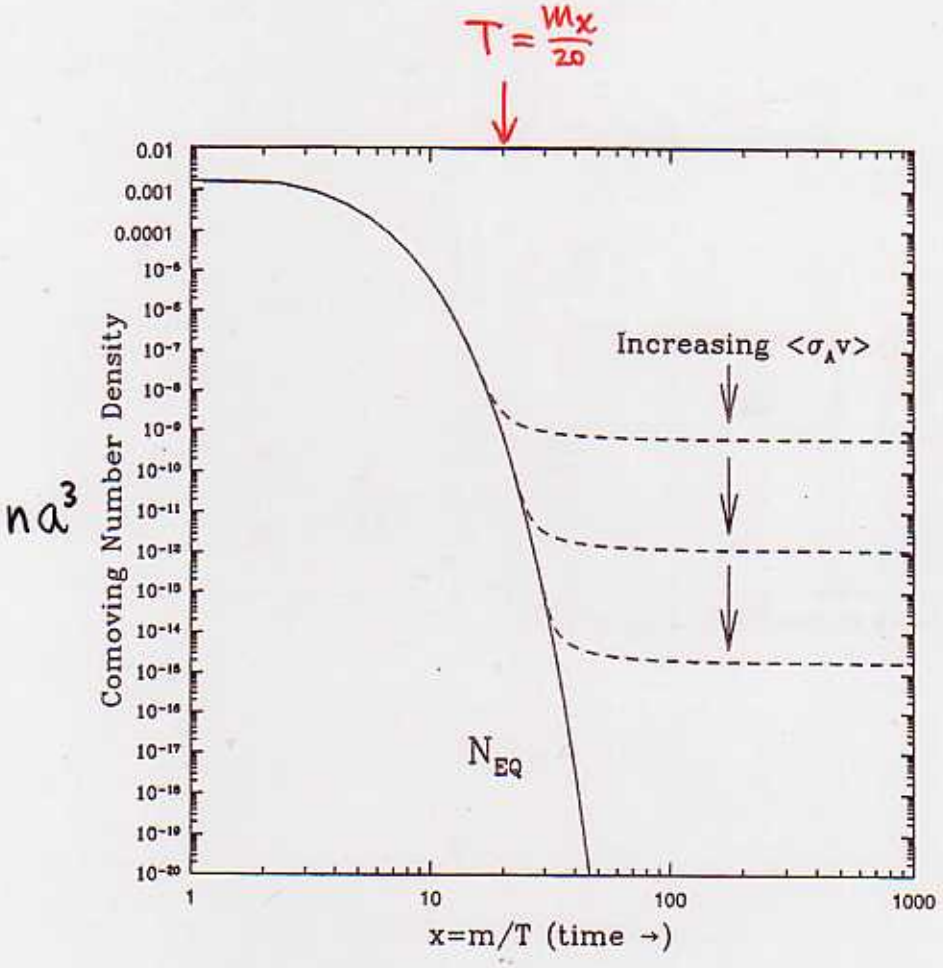

$$\frac{dn}{dt} + 3Hn = -\langle\sigma v\rangle(n^2 - n_{eq}^2)$$

$$H \leftrightarrow \langle\sigma v\rangle n \equiv \Gamma$$

Fig. 4. Comoving number density of a WIMP in the early Universe. The dashed curves are the actual abundance, and the solid curve is the equilibrium abundance. From [31].

interaction rate $\Gamma \sim n\sigma v$

expansion rate $H \sim T^2/M_{PL}$ (RD)

$\Gamma > H$ thermal

$n_{eq} \sim (mT)^{3/2} e^{-m/T}$ $(T \ll m)$

$\Gamma < H$ decoupled (freeze out)

$T_f \approx m_x/20$

Cross section $\sigma(\chi\chi \to \text{all})$

Process	s-channel	t & u-channel
$\chi\chi \to f\bar{f}$	$h,\ H,\ A,\ Z$	$\tilde{f}_{1-6}$
$\chi\chi \to hh, hH, HH$	$h,\ H$	χ^0_{1-4}
hA, HA	$A,\ Z$	χ^0_{1-4}
AA	$h,\ H$	χ^0_{1-4}
H^+H^-	$h,\ H,\ Z$	$\chi^{\pm}_{1,2}$
$\chi\chi \to W^+W^-$	$h,\ H,\ Z$	$\chi^{\pm}_{1,2}$
ZZ	$h,\ H$	χ^0_{1-4}
$\chi\chi \to Zh, ZH$	$A,\ Z$	χ^0_{1-4}
ZA	$h,\ H$	χ^0_{1-4}
$W^{\pm}H^{\mp}$	$h,\ H,\ A$	$\chi^{\pm}_{1,2}$

Resonance (pole) at $2m_\chi \approx m_A, \cdots$

$\chi \sim \tilde{B}\ (M_1 \ll \mu) \longrightarrow \sigma$ small

$\chi \sim \tilde{H}\ (M_1 \gg \mu) \longrightarrow \sigma$ large

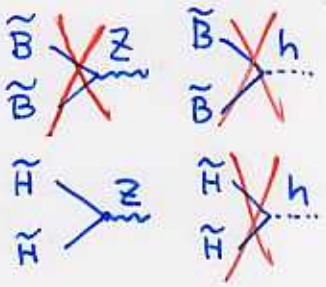

$\chi \sim (\tilde{B}, \tilde{W}^3, \tilde{H}^0_1, \tilde{H}^0_2)$

$\frac{1}{2}M_1\tilde{B}\tilde{B}$ $\quad \frac{1}{2}M_2\tilde{W}^3\tilde{W}^3$ $\quad \mu\tilde{H}^0_1\tilde{H}^0_2$

CMSSM
$M_1 \approx \frac{1}{2}M_2$

$$J(x_f) = \int_0^{x_f} dx \langle \sigma v \rangle$$

T.N.–Roszkowski–Ruiz
(JHEP0108)

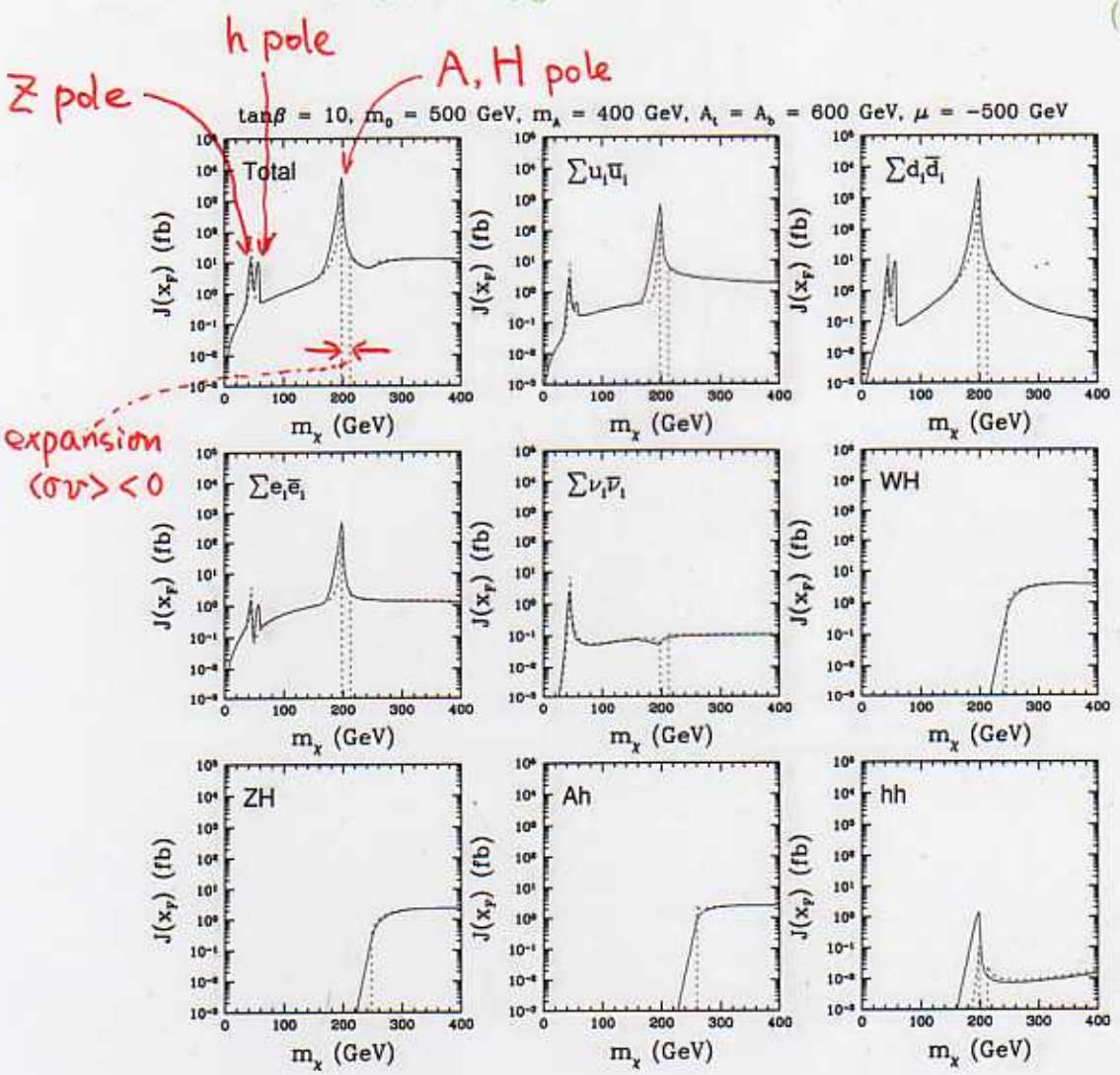

Figure 1: The total value of $J(x_f)$, Eq. (5), and several partial contribution are shown in separate windows as a function of m_χ for $\tan\beta = 10$, $m_0 \equiv m_Q = m_U = m_D = m_L = m_E = 500\,\text{GeV}$, $m_A = 400\,\text{GeV}$, $A_t = A_b = 600\,\text{GeV}$ and $\mu = -500\,\text{GeV}$. The solid lines represent the exact results, while the dotted ones correspond to the expansion (13. Notice that the final states $W^\pm H^\mp$, ZH^0 and Ah, once kinematically allowed, give comparable contributions to the $f\bar{f}$ channels.

WH can be dominant. (cf. $f\bar{f}, WW$)

■ Thermal average $\langle \sigma v \rangle$

[1] Exact formula

Gondolo–Germini (1991)

$$\langle \sigma v_{\rm rel} \rangle = \frac{\int d^3p_1 d^3p_2\, \sigma v_{\rm rel}\, e^{-E_1/T} e^{-E_2/T}}{\int d^3p_1 d^3p_2\, e^{-E_1/T} e^{-E_2/T}}$$

$$= \frac{1}{8m_\chi^4 T K_2^2(\frac{m_\chi}{T})} \int_{4m_\chi^2}^{\infty} ds\; \sigma \sqrt{s}(s-4m_\chi^2) K_1\left(\frac{\sqrt{s}}{T}\right)$$

$$\sim \int_{4m_\chi^2}^{4m_\chi^2(1+\epsilon)} ds\; \sigma \cdot F(s)$$

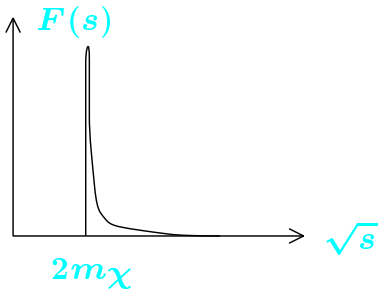

[2] Expansion

$$\langle \sigma v_{\rm rel} \rangle = a + bx, \quad x = T/m_\chi$$

$$a = w(4m_\chi^2),\ b = -\tfrac{3}{2}(2w - w')|_{s=4m_\chi^2},\ w(s) = \frac{1}{2m_\chi^2}\sqrt{s(s-4m_\chi^2)}\sigma(s)$$

Exact vs Expansion

Naively, "expansion" should converge quickly,
because $F(s)$ decays quickly.
However, this is not necessarily true
when σ varies rapidly with s.

[e.g. near resonance,
threshold of new channel]

Griest–Seckel (1991)

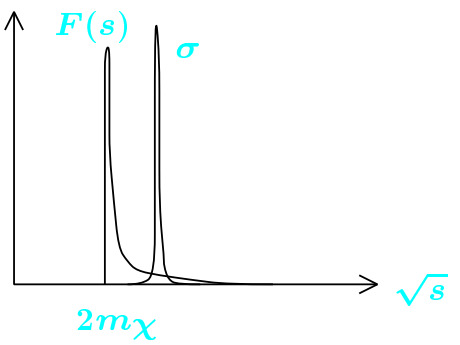

T.N.–Roszkowski–Ruiz
(JHEP0105)

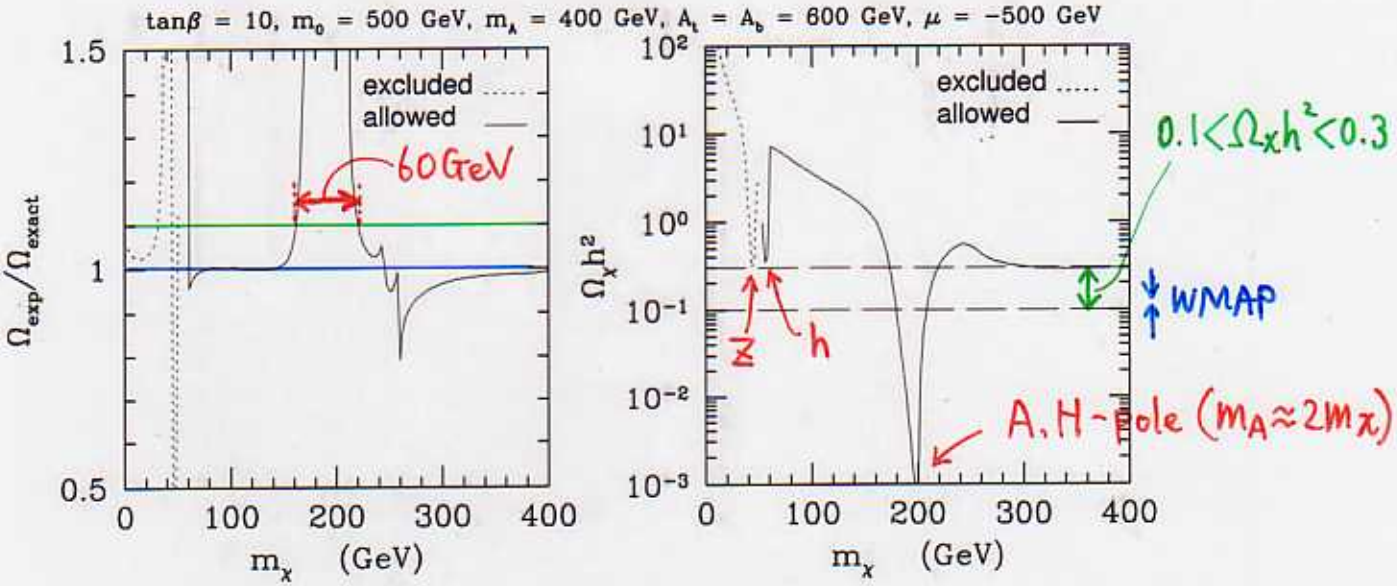

Figure 4: The ratio $\Omega_{\rm exp}/\Omega_{\rm exact}$ (a) and the relic density $\Omega_\chi h^2$ (b) for the same choice of parameters as in Fig. 1. The solid (dotted) curves are allowed (excluded) by current experimental constraints. In window (a) the relic aboundance in both cases is computed by solving Eq. (3) iteratively and using Eq. (4). In window (b) we show $\Omega_\chi h^2$ is computed using our numerical code. The band between the two horizontal dashed lines corresponds to the cosmologically favoured range $0.1 < \Omega_\chi h^2 < 0.3$.

usual expansion:

large error over sizable range of m_χ

Freeze-out temperature

T.N.–Roszkowski–Ruiz (JHEP0105)

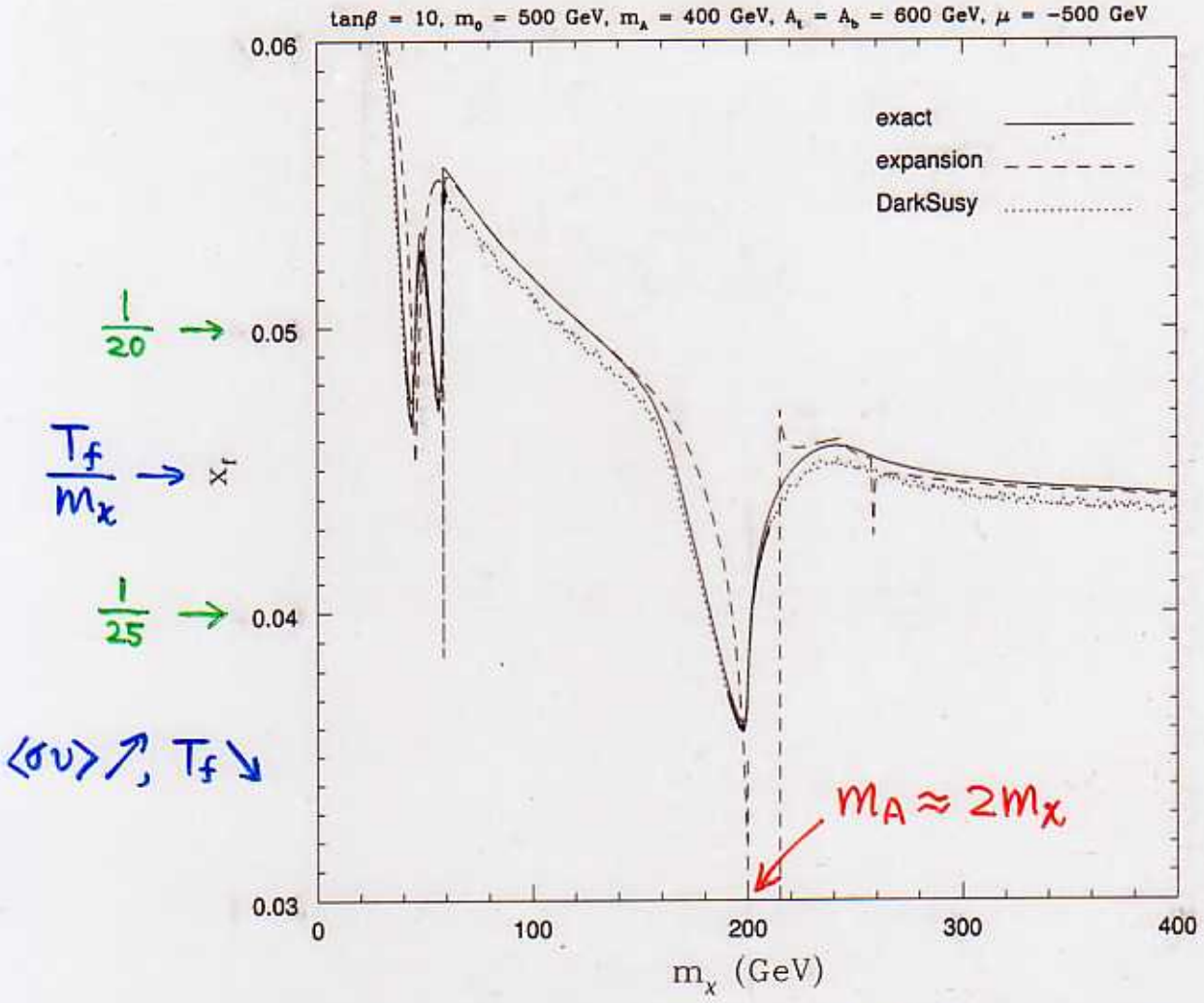

Figure 3: The freeze-out point x_f as a function of m_χ. The solid and dashed lines corresponds to the iterative procedure (3) with $\langle\sigma v_{\text{Møl}}\rangle$ computed exactly (6) and in terms of the expansion (13), respectively. For comparison, the dotted line has been obtained using DarkSusy.

Approximate solution to the Boltzmann eq.

$$\rho_\chi = \frac{1.66}{M_{Pl}} \left(\frac{T_\chi}{T_\gamma}\right)^3 T_\gamma^3 \sqrt{g_*} \frac{1}{\int_0^{x_f} dx \langle\sigma v\rangle}$$

where

$$x_f^{-1} = \ln\left(\frac{m_\chi}{2\pi^3}\sqrt{\frac{45}{2g_* G_N}}\langle\sigma v\rangle_{x_f} x_f^{1/2}\right)$$

Coannihilation

Griest–Seckel (1991)

If NLSP (χ') is nearly degenerate with LSP ($m_{\chi'} \lesssim 1.1 m_\chi$), then χ' is as abundant as χ at $T_f \approx \frac{m_\chi}{20}$.

$\longrightarrow$ $\left.\begin{array}{l}\sigma(\chi\chi' \to f f') \\ \sigma(\chi'\chi' \to f f')\end{array}\right\}$ should be included.

↖ can be $\gg \sigma(\chi\chi \to f f')$

(f, f': SM particles)

$\chi f \leftrightarrow \chi' f'$ is much faster than $\chi\chi \leftrightarrow f f'$.

↑ ↑

Reaction rate

$r_{\chi f} \sim n_\chi n_f \sigma_{\chi f}$ $\ggg$ $r_{\chi\chi} \sim n_\chi n_\chi \sigma_{\chi\chi}$

$\sim \sigma_{\chi f} \exp\left(-\frac{m_\chi}{T}\right)$ $\sim \sigma_{\chi\chi} \exp\left(-\frac{2m_\chi}{T}\right)$

- Boltzmann eq. with coannihilation

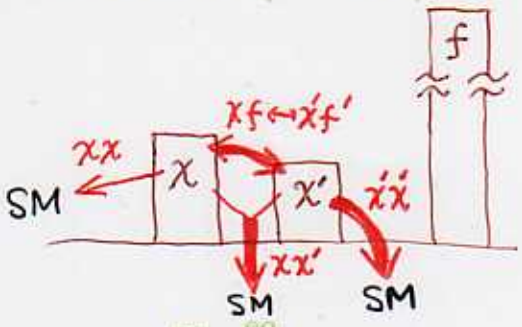

Replacements

$$\begin{cases} n_\chi & \to & n = \sum_i n_i \\ \langle\sigma v\rangle & \to & \langle\sigma_{\rm eff}\, v\rangle = \sum_{i,j} \langle\sigma_{ij} v_{ij}\rangle \frac{n_i^{\rm eq}}{n^{\rm eq}} \frac{n_j^{\rm eq}}{n^{\rm eq}} \end{cases}$$

↓

$$\frac{dn}{dt} + 3Hn = -\langle\sigma_{\rm eff}\, v\rangle (n^2 - n_{\rm eq}^2)$$

$\sigma \to \sigma_{\rm eff}$: enhanced by coann.

- CMSSM:

$\chi' = \tilde{\tau}_1,\ \chi_1^\pm, \chi_2^0$

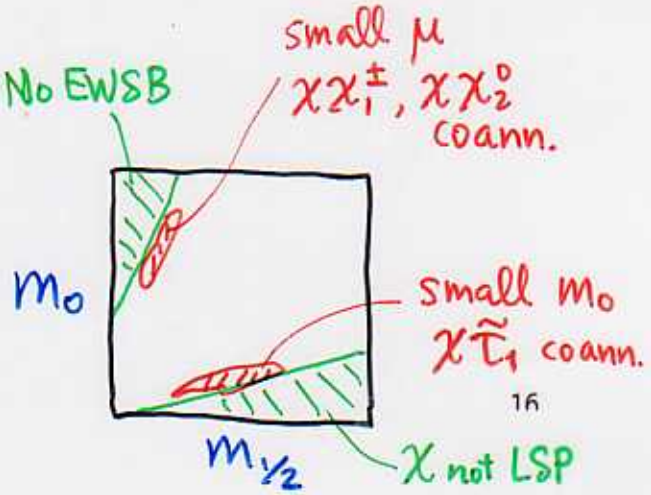

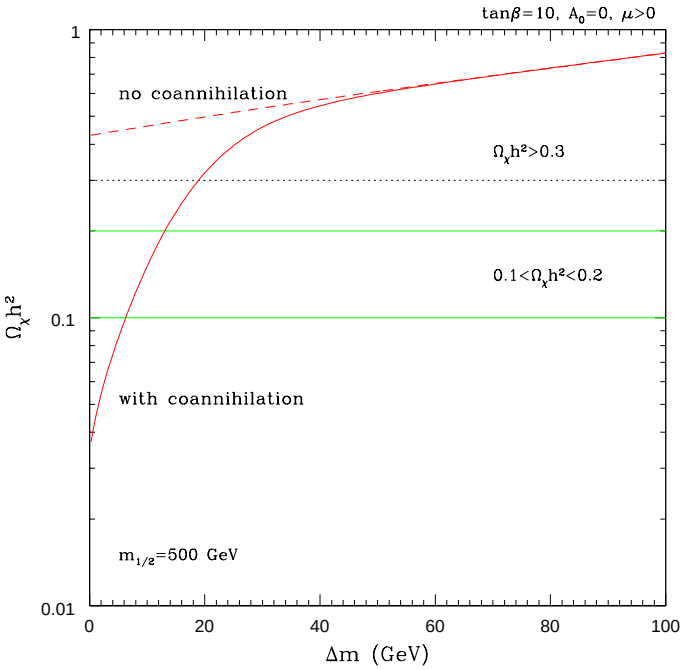

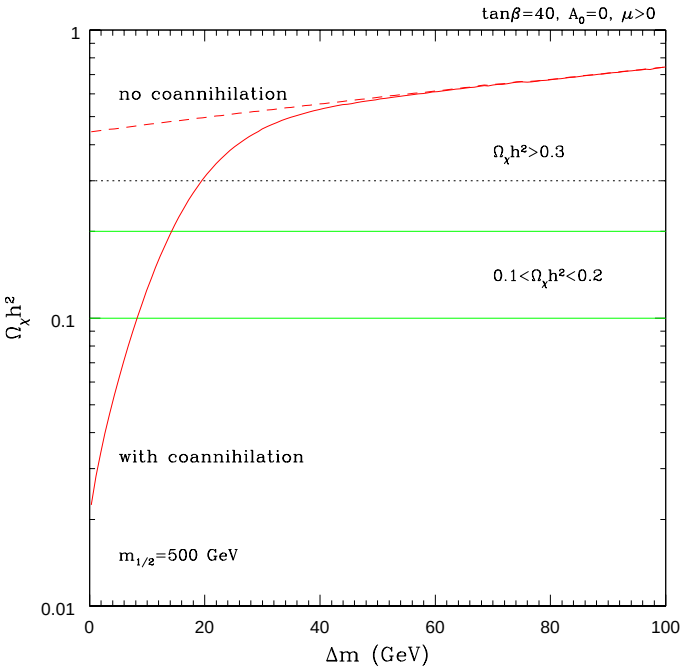

$$\Delta m = m_{\tilde{\tau}_1} - m_{\chi}$$

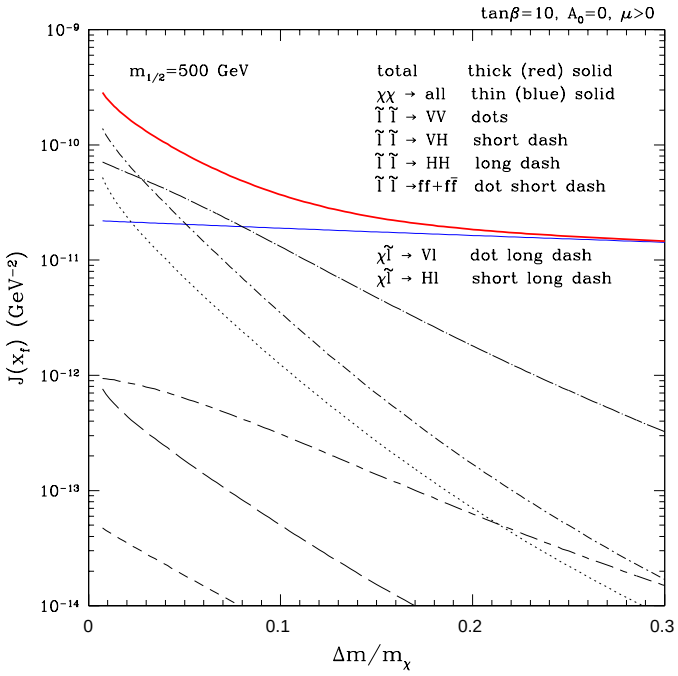

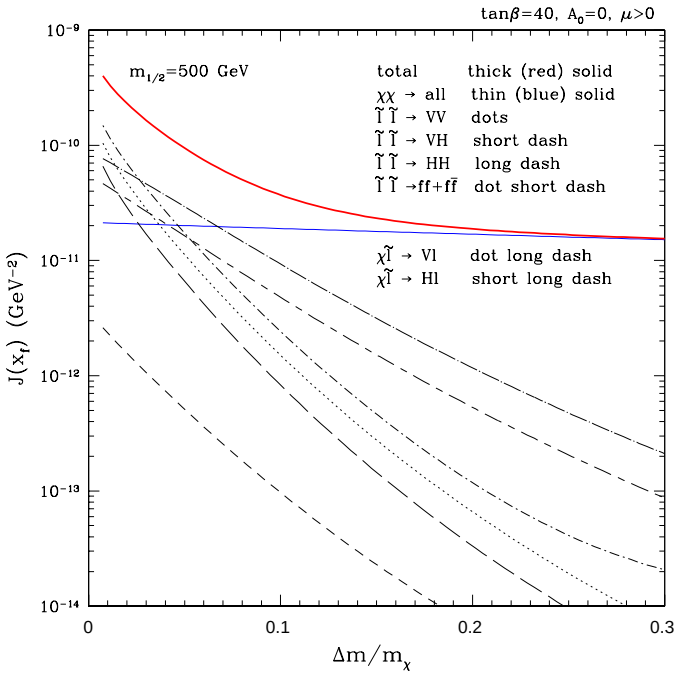

$$J(x_f) = \int_0^{x_f} dx \langle \sigma v \rangle$$

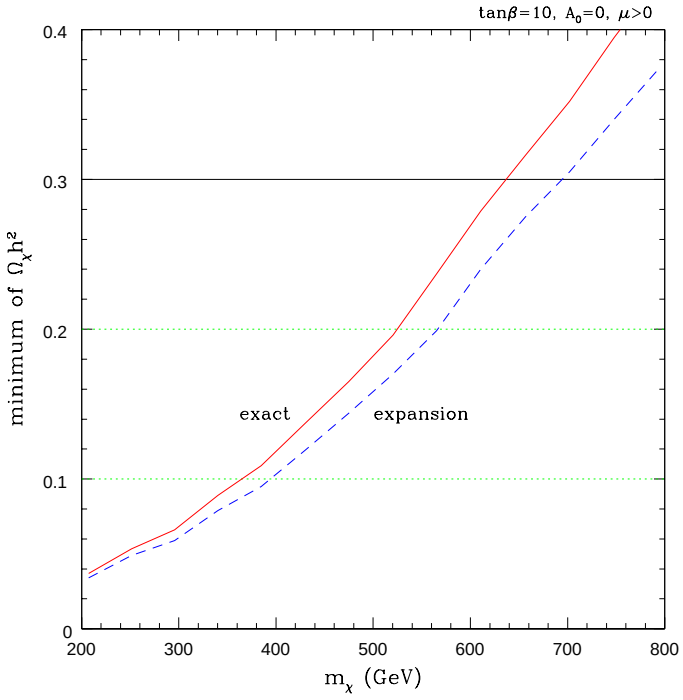
tanβ=10, A0=0, μ>0
minimum of Ωχh²
0.4
0.3
0.2
0.1
0
200
300
400
500
600
700
800
exact
expansion
mχ (GeV)

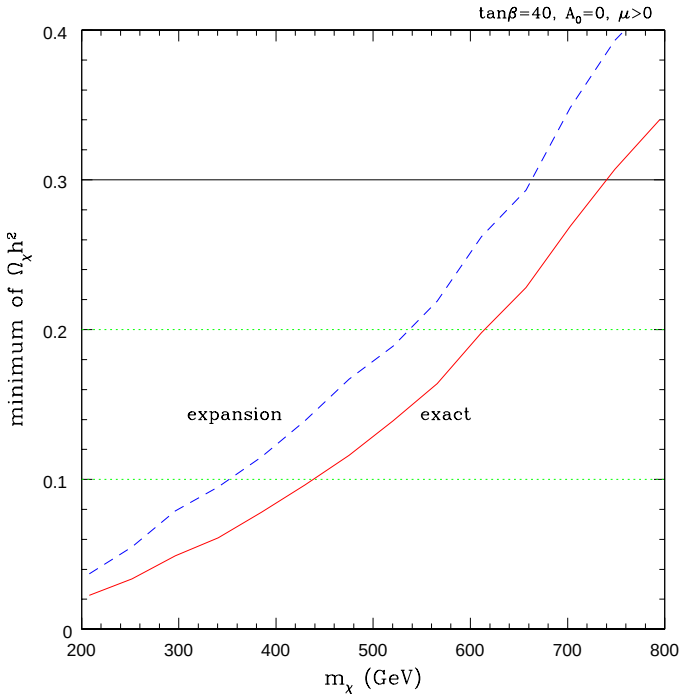
tanβ=40, A0=0, μ>0
minimum of Ωχh²
0.4
0.3
0.2
0.1
0
200
300
400
500
600
700
800
expansion
exact
mχ (GeV)

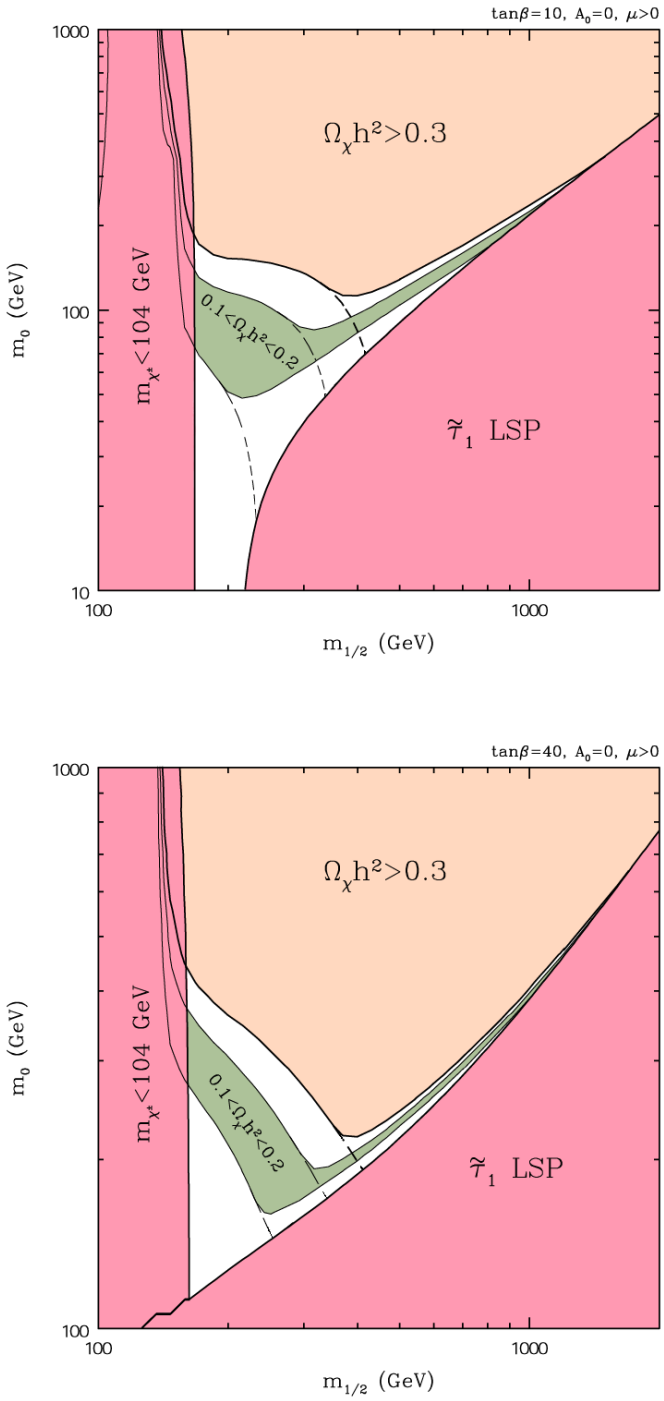

Figure 6: Contours of $\Omega_\chi h^2$ in the plane $(m_{1/2}, m_0)$ for $\tan\beta = 10$ (upper window) and $\tan\beta = 40$ (lower window), and for $A_0 = 0$, $\mu > 0$, $m_t^{\rm pole} = 175\,{\rm GeV}$ and $m_b(m_b)^{\overline{\rm MS}}_{\rm SM} = 4.20\,{\rm GeV}$. The red regions bands are excluded by chargino searches at LEP and corresponds to the lighter stau being the LSP. The light orange regions of $\Omega_\chi h^2 > 0.3$ are excluded by cosmology while the narrow green bands correspond to the expected range $0.1 < \Omega_\chi h^2 < 0.2$. Also shown are the semi–oval contours of $\Omega_\chi h^2$ in the absence of coannihilation.

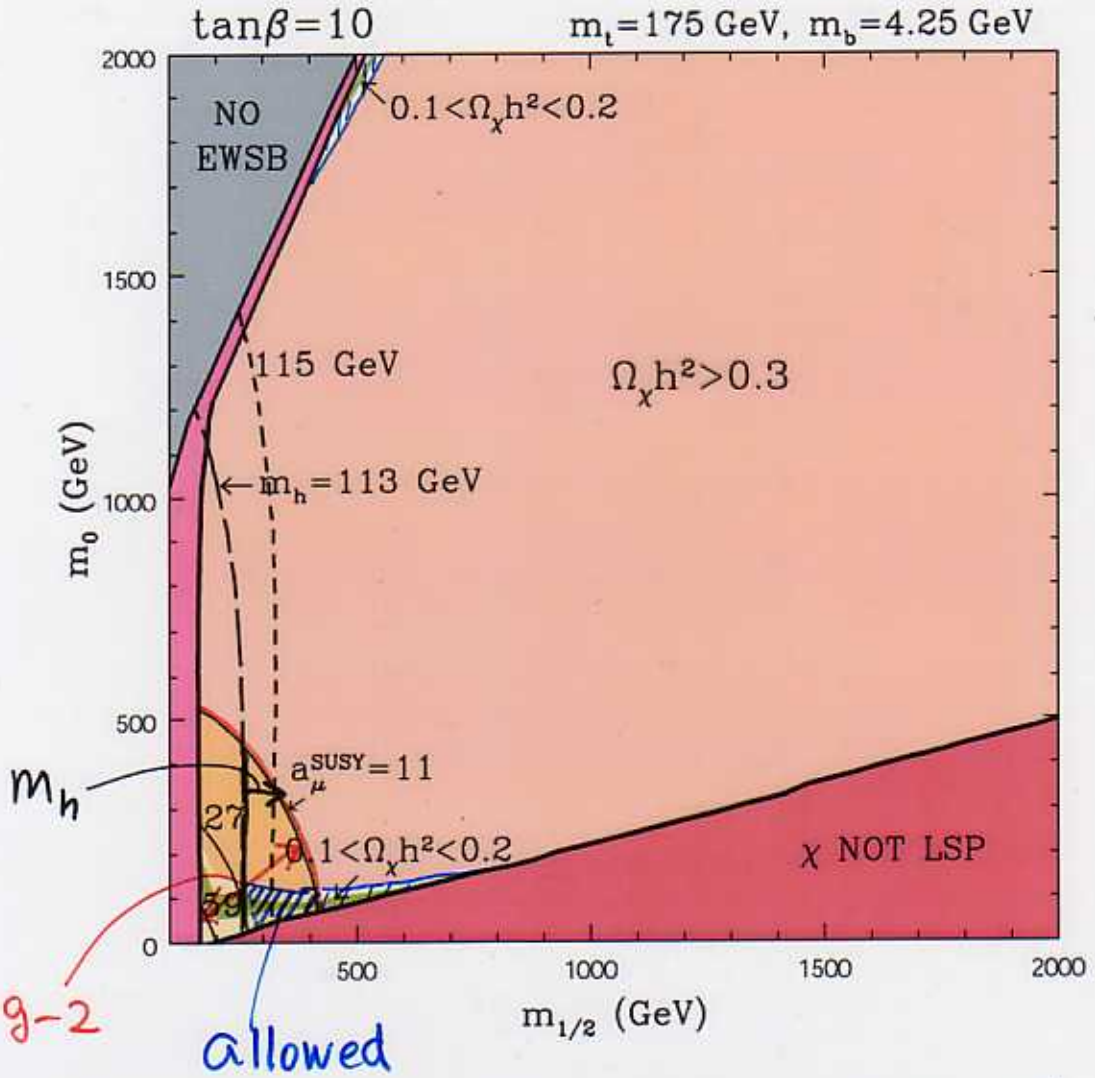

Figure 1: The plane $(m_{1/2}, m_0)$ for $\tan\beta = 10$, $A_0 = 0$, $\mu > 0$ and for $m_t \equiv m_t^{\rm pole} = 175\,{\rm GeV}$ and $m_b \equiv m_b(m_b)^{\overline{\rm MS}}_{\rm SM} = 4.25\,{\rm GeV}$. The light red bands on the left are excluded by chargino searches at LEP. In the grey wedge in the left-hand corner electroweak symmetry breaking conditions are not satisfied. The dark red region denoted 'χ NOT LSP' corresponds to the lighter stau being the LSP. The large light orange regions of $\Omega_\chi h^2 > 0.3$ are excluded by cosmology while the narrow green bands correspond to the expected range $0.1 < \Omega_\chi h^2 < 0.2$. Also shown are the semi-oval contours of $a_\mu^{\rm SUSY} \equiv \Delta a_\mu^{\rm SUSY}/10^{-10}$ favored by the anomalous magnetic moment of the muon measurement at 2σ CL ($a_\mu^{\rm SUSY} = 11, 75$) and 1σ CL ($a_\mu^{\rm SUSY} = 27, 59$). The 2σ range is shown in dark yellow. The three lines in the figure correspond respectively to $a_\mu^{\rm SUSY} = 11, 27$ and 59, when moving towards the origin. The lines of the lightest Higgs scalar mass $m_h = 113\,{\rm GeV}$ and 115 GeV are denoted by short and long-dash lines, respectively.

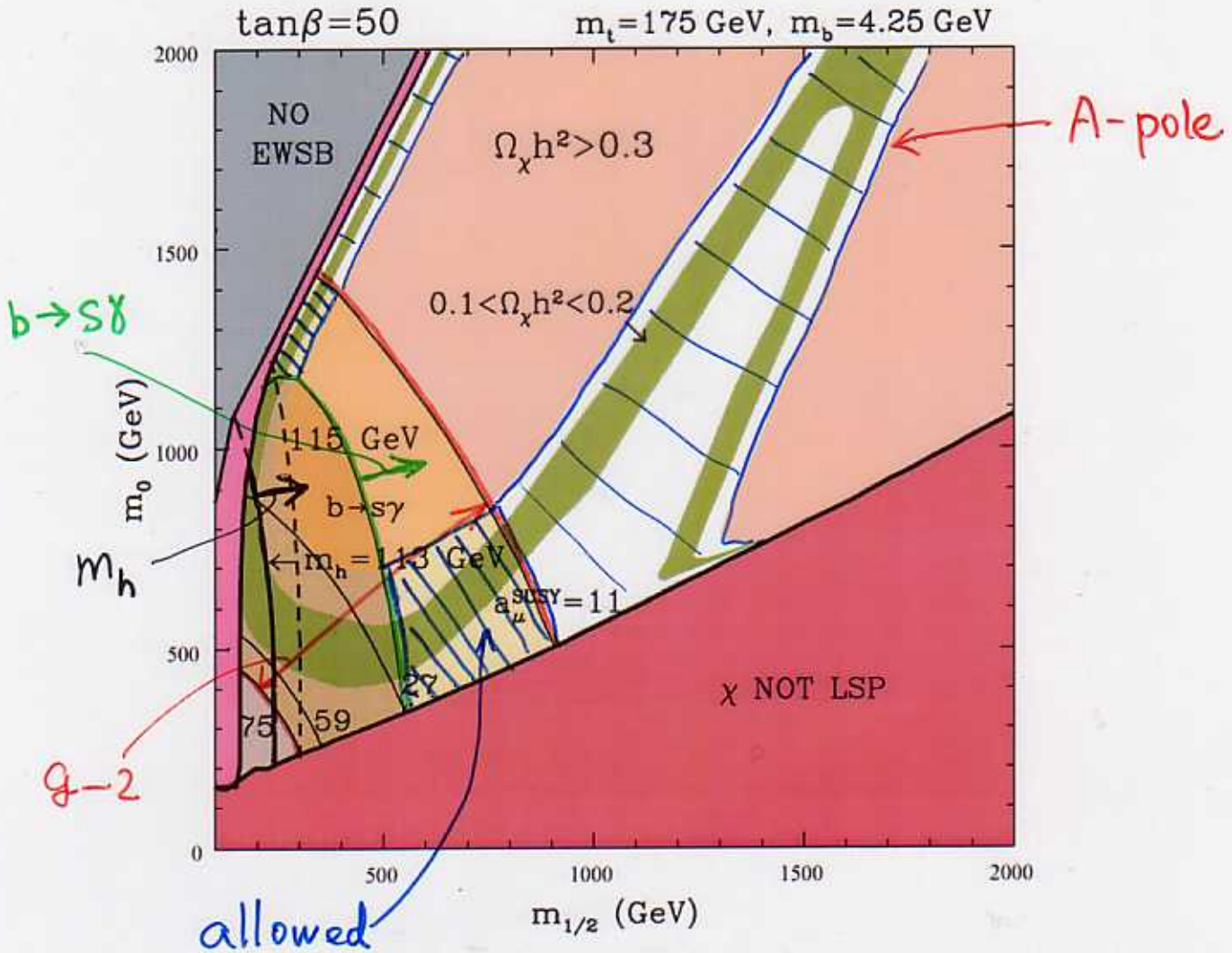

Figure 3: The same as in Fig. 2 but for $\tan\beta = 50$. The green band of the expected range $0.1 < \Omega_\chi h^2 < 0.2$ has now changed considerably due to the appearance of a wide resonance $\chi\chi \to A \to f\bar{f}$. The white areas closer (further away) from the axes correspond to $\Omega_\chi h^2 < 0.1$ ($0.2 < \Omega_\chi h^2 < 0.3$).

Allowed regions grow significantly

as $\tan\beta \to 50$ (A–pole effect)

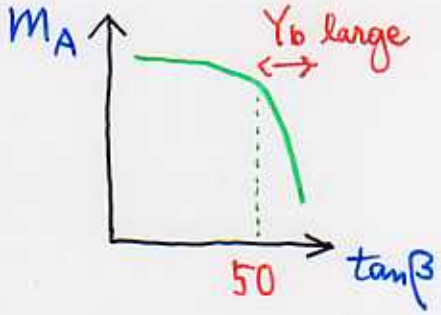

WMAP : $\Omega h^2 = 0.094 - 0.129$ (1σ)

$\Omega h^2 = 0.1 - 0.3$

Ellis–Olive–Santoso–Spanos (2003)

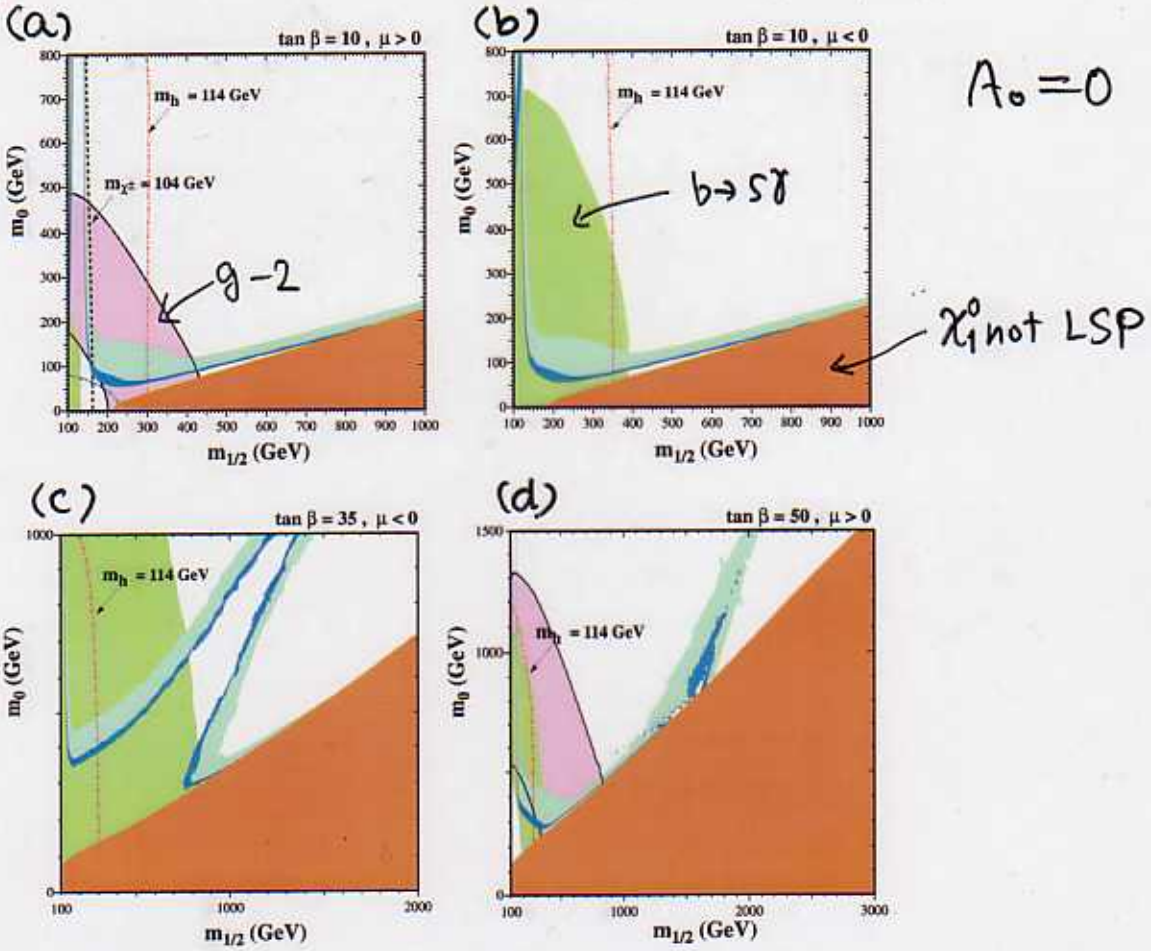

$A_0 = 0$

Figure 1: *The* $(m_{1/2}, m_0)$ *planes for (a)* $\tan\beta = 10, \mu > 0$, *(b)* $\tan\beta = 10, \mu < 0$, *(c)* $\tan\beta = 35, \mu < 0$, *and (d)* $\tan\beta = 50, \mu > 0$. *In each panel, the region allowed by the older cosmological constraint* $0.1 \leq \Omega_\chi h^2 \leq 0.3$ *has medium shading, and the region allowed by the newer cosmological constraint* $0.094 \leq \Omega_\chi h^2 \leq 0.129$ *has very dark shading. The disallowed region where* $m_{\tilde{\tau}_1} < m_\chi$ *has dark (red) shading. The regions excluded by* $b \to s\gamma$ *have medium (green) shading, and those in panels (a,d) that are favoured by* $g_\mu - 2$ *at the 2-*σ *level have medium (pink) shading. A dot-dashed line in panel (a) delineates the LEP constraint on the* $\tilde{e}$ *mass and the contours* $m_{\chi^\pm} = 104$ *GeV (*$m_h = 114$ *GeV) are shown as near-vertical black dashed (red dot-dashed) lines in panel (a) (each panel).*

Allowed "line"

Ellis-Olive-Santoso-Spanos (2003)

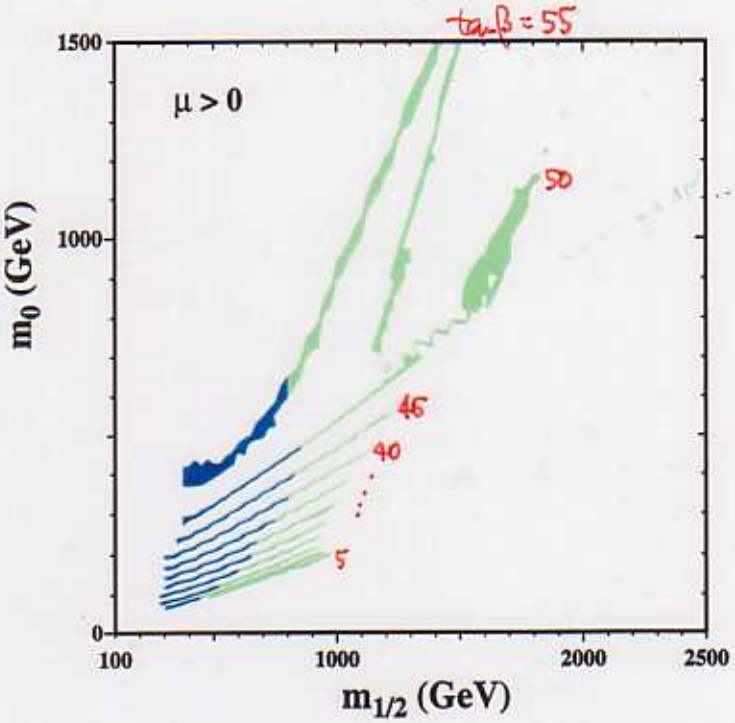

g-2 imposed

WMAP

Figure 2: *The strips display the regions of the* $(m_{1/2}, m_0)$ *plane that are compatible with* $0.094 < \Omega_\chi h^2 < 0.129$ *and the laboratory constraints for* $\mu > 0$ *and* $\tan\beta = 5, 10, 15, 20, 25, 30, 35, 40, 45, 50, 55$. *The parts of the strips compatible with* $g_\mu - 2$ *at the 2-*σ *level have darker shading.*

are considerably narrower than the spacing between them, though any intermediate point in the $(m_{1/2}, m_0)$ plane would be compatible with some intermediate value of $\tan\beta$. The right (left) ends of the strips correspond to the maximal (minimal) allowed values of $m_{1/2}$ and hence m_χ[3]. The lower bounds on $m_{1/2}$ are due to the Higgs mass constraint for $\tan\beta \leq 23$, but are determined by the $b \to s\gamma$ constraint for higher values of $\tan\beta$. The upper bound on $m_{1/2}$ for $\tan\beta \gtrsim 50$ is clearly weaker, because of the rapid-annihilation regions.

Also shown in Fig. 2 in darker shading are the restricted parts of the strips that are compatible with the BNL measurement of $g_\mu - 2$ at the 2-σ level, if low-energy e^+e^- data are used to calculate the Standard Model contribution [17]. If this constraint is imposed, the range of $m_{1/2}$ is much reduced for any fixed value of $\tan\beta$, and in particular the upper bound on $m_{1/2}$ is significantly reduced, particularly for $\tan\beta \gtrsim 50$. However, there is in

[3]The droplets in the upper right of the figure are due to coannihilations when $\tilde{\tau}$ is sitting on the Higgs pole. Here this occurs at $\tan\beta = 45$.

Birkedal-Hansen - Nelson (2003)

$$r = \frac{M_2}{M_1}$$

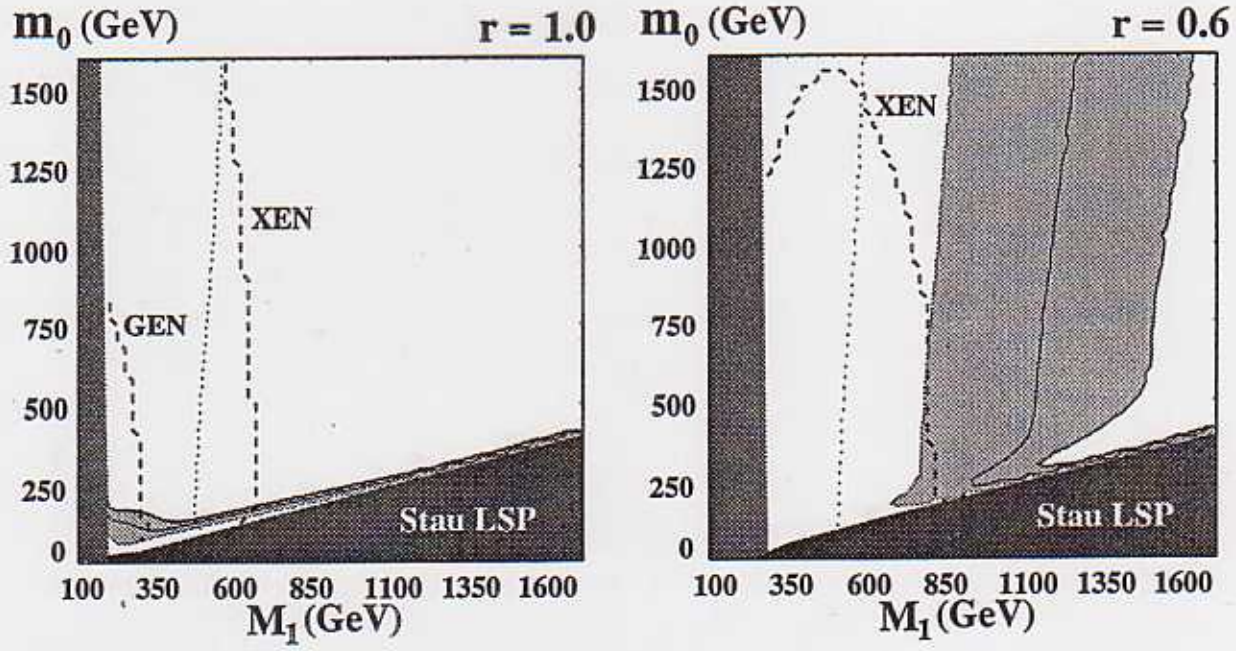

FIG. 1: **Neutralino Relic Densities for** $\tan\beta = 5$. The preferred neutralino relic density regions (light shading) are displayed for $r = 1$ (left panel) and for $r = 0.6$ (right panel). Dark shaded regions in the lower right are excluded due to a charged LSP. Medium shaded regions on the left are excluded by LEP bounds on the chargino mass. The Higgs mass contour of $m_h = 113$ GeV is given by the dotted vertical line. The dashed contours are a rough estimate of the direct detection reach of the GENIUS ("GEN") and XENON ("XEN") experiments.

III. Direct detection

■ Calculation of direct detection rate

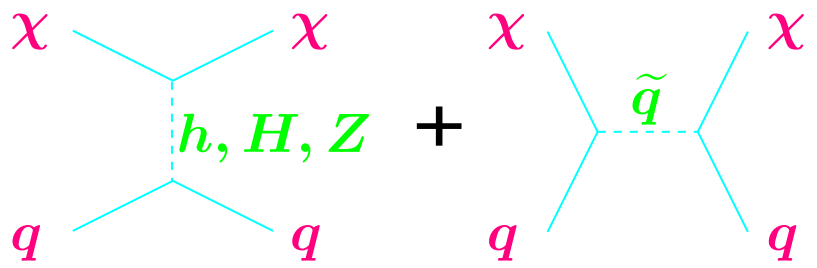

Goodman–Witten (1985)

Drees–Nojiri (1993)

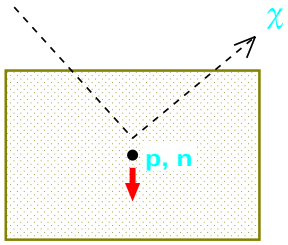

Cross section of $\chi p \longrightarrow \chi p$

$$\sigma_p = \sigma_p^{\rm SI} + \sigma_p^{\rm SD}$$

spin indep. $(h,\ H,\ \tilde{q})$ — spin dep. $(Z,\ \tilde{q})$

$$\mathcal{L}_{\rm eff} = f_q\, \overline{\chi}\chi\, \overline{q}q + \cdots$$

$$\Downarrow \quad \langle p|\overline{q}q|p\rangle\text{: input}$$

$$\mathcal{L}_{\rm eff} = f_p\, \overline{\chi}\chi\, \overline{p}p \longrightarrow \sigma_p^{\rm SI} = \frac{4}{\pi}\mu_p^2 f_p^2,\ \ \mu_p = \frac{m_\chi m_p}{m_\chi + m_p}$$

- H, h: comparable
- $\sigma_p^{\rm SI} \leftrightarrow \sigma_{\chi\chi}^{\rm ann}$

  $m_A \searrow$, $\sigma_p^{\rm SI} \nearrow$
- $\tan\beta \nearrow$, $\sigma_p^{\rm SI} \nearrow$

Parameters

$$
\begin{aligned}
\mathbf{50}\,\mathrm{GeV} \leq \quad & M_2 & \leq \mathbf{2}\,\mathrm{TeV} \\
\mathbf{50}\,\mathrm{GeV} \leq \quad & |\mu| & \leq \mathbf{2}\,\mathrm{TeV}\ (\mathbf{4}\,\mathrm{TeV}) \\
\mathbf{50}\,\mathrm{GeV} \leq \quad & \widetilde{m}_{\tilde{l}} & \leq \mathbf{2}\,\mathrm{TeV}\ (\mathbf{4}\,\mathrm{TeV}) \\
\mathbf{200}\,\mathrm{GeV} \leq \quad & \widetilde{m}_{\tilde{q}} & \leq \mathbf{2}\,\mathrm{TeV}\ (\mathbf{4}\,\mathrm{TeV}) \\
\mathbf{90}\,\mathrm{GeV} \leq \quad & m_A & \leq \mathbf{2}\,\mathrm{TeV} \\
\mathbf{0} \leq \quad & |A_{t,b}| & \leq \mathbf{1}\,\mathrm{TeV} \\
\mathbf{5} \leq \quad & \tan\beta & \leq \mathbf{65}
\end{aligned}
$$

with GUT relations for gaugino masses

$(\longrightarrow M_1 = \frac{5}{3}\tan^2\theta_W M_2)$

Kim–T.N.–Roszkowski–Ruiz (JHEP0212)

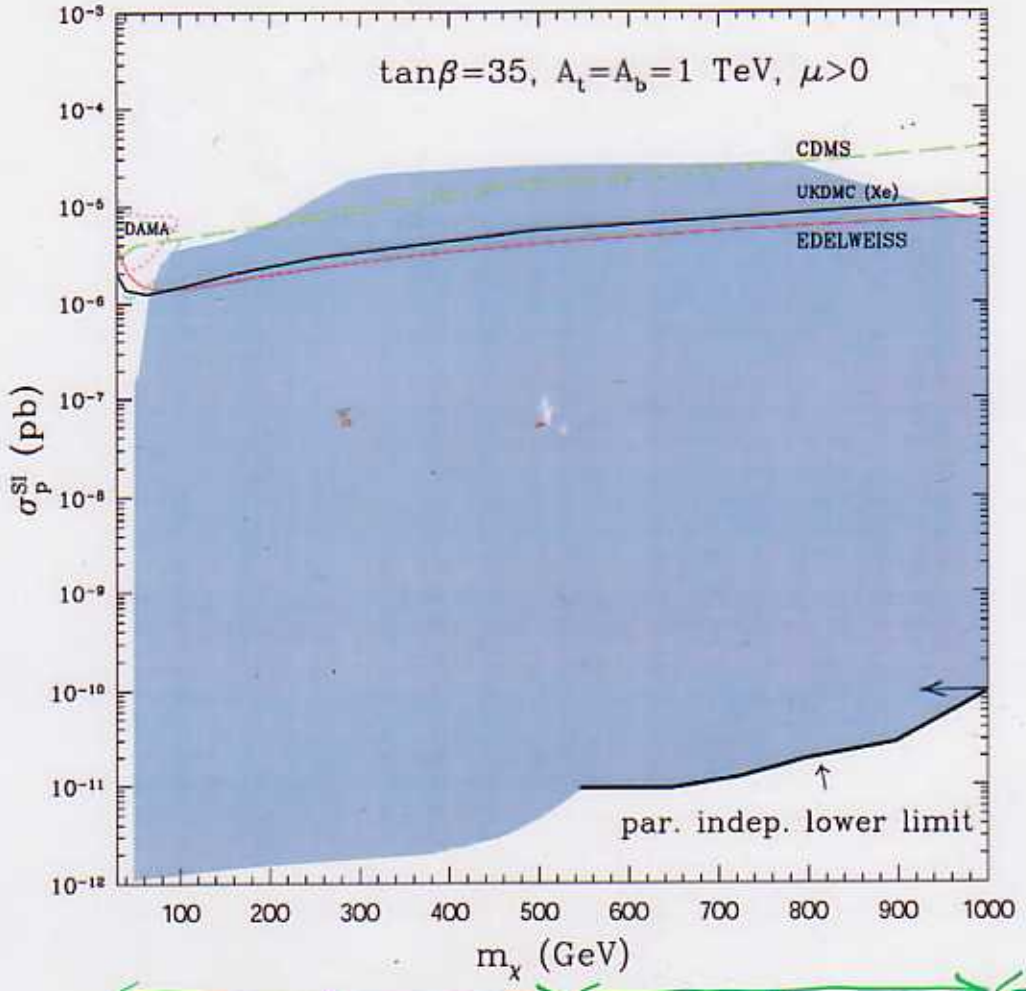

Figure 1: Ranges of $\sigma_p^{\rm SI}$ in the general MSSM *vs.* m_χ for $\tan\beta = 35$, $A_t = A_b = 1\,\text{TeV}$ and $\mu > 0$, which are allowed by the bounds from colliders, $b \to s\gamma$ and $0.1 < \Omega_\chi h^2 < 0.2$, but not from $(g-2)_\mu$. Also marked are some results of recent experimental WIMP searches. The thick black line (and a left–pointing arrow) indicates a *parameter–independent* lower bound on $\sigma_p^{\rm SI}$ for $550\,\text{GeV} < m_\chi < 1020\,\text{GeV}$. No similar bound can be set for lower m_χ because of the neutralino–slepton coannihilation effect, as explained in the text.

- small σ_p with $m_H, m_{\tilde{q}} \to \infty$
- ★ with coann ($m_{\tilde{\ell}} \to m_\chi$)

lower bound on σ_p by ★

★ with $\tilde{H}$-like LSP, $M_2 \to \infty$, $\chi\chi H \to 0$

Too small Ωh^2 with $\tilde{H}$-like LSP

[$\mu < 0$ No lower bound on σ_p^{SI} cancellation]

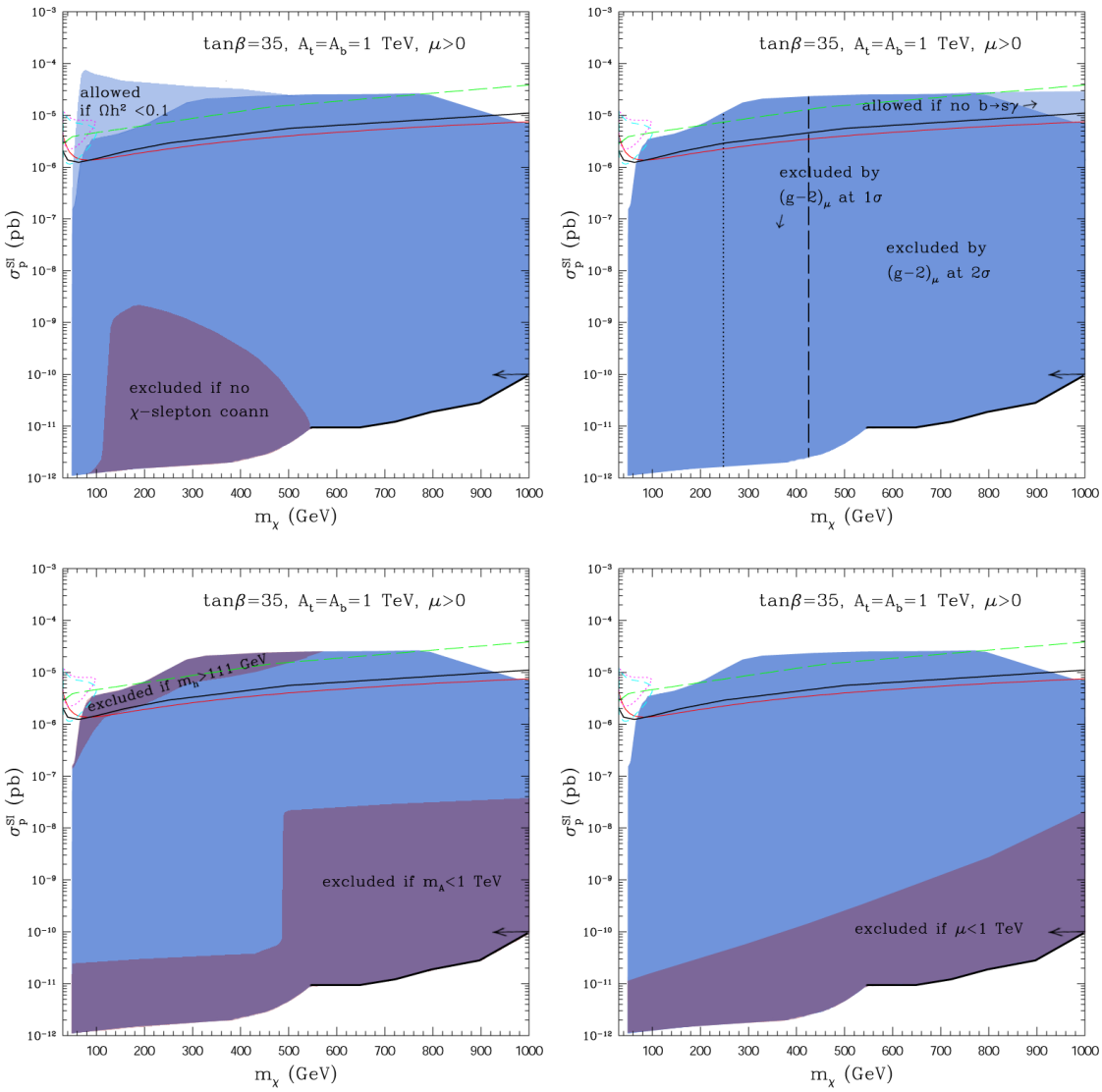

Figure 2: Sensitivity of the upper and lower limits on σ_p^{SI} in Fig. 1 to various assumptions and constraints. Upper left window: the light blue region would be allowed if $\Omega_\chi h^2 < 0.1$. The dark–red region would be excluded if one neglected the effect of neutralino–slepton coannihilation. Upper right window: the light blue region would be allowed if one lifted the constraint from $b \to s\gamma$. The regions to the right of the vertical dotted (dashed) lines are excluded by imposing current $1\,\sigma$ ($2\,\sigma$) CL bound from $(g-2)_\mu$. Lower left window: the upper dark–red region would be excluded by assuming $m_h > 111\,\mathrm{GeV}$ for all m_A (*i.e.*, by neglecting a window of lighter m_h which is still allowed for $m_A < 120\,\mathrm{GeV}$). Also shown in this window is the effect of restricting $m_A < 1\,\mathrm{TeV}$. Lower right window: the same as for m_A but for μ.

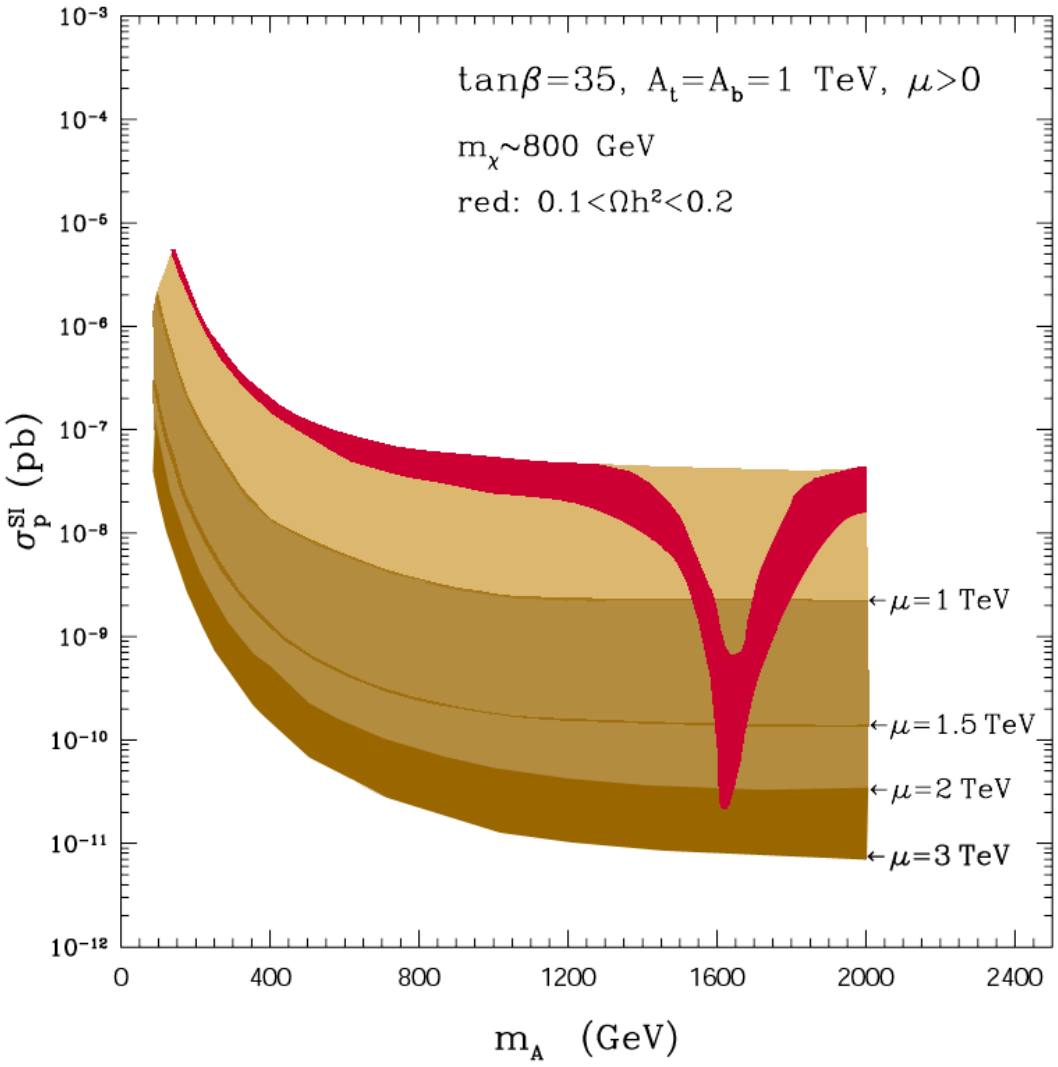

Figure 3: Sensitivity of $\sigma_p^{\rm SI}$ to m_A and μ for the case of Fig. 1. We concentrate on the region of parameter space where $m_\chi \sim 800\,{\rm GeV}$. The whole marked region is consistent with all the constraints from colliders and $b \to s\gamma$. By further imposing the constraint $0.1 < \Omega_\chi h^2 < 0.2$ one selects only the red region. Near the resonance $m_A \simeq 2m_\chi$, significantly smaller values of $\sigma_p^{\rm SI}$ become allowed by $0.1 < \Omega_\chi h^2 < 0.2$, (mostly in the increasingly pure bino region), but become eventually limited from below, independently of increasing the maximum allowed value of μ.

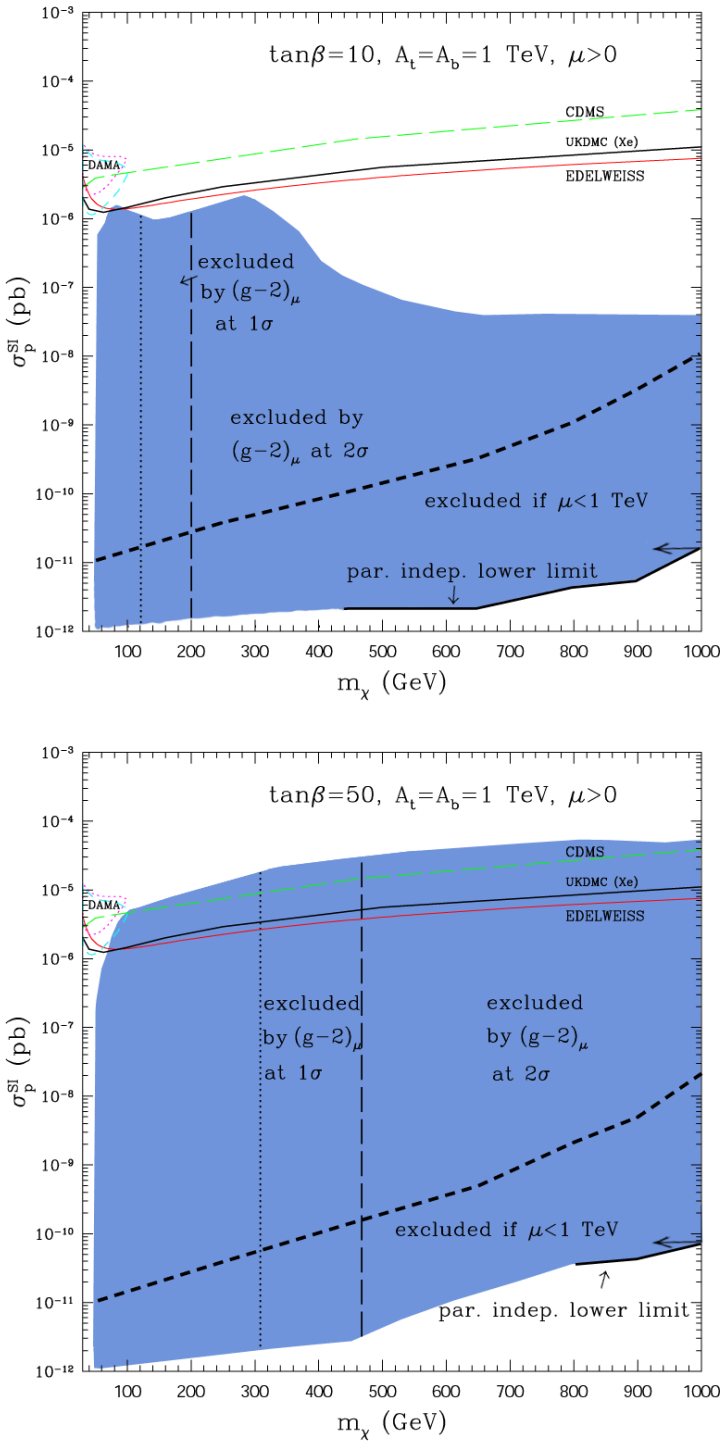

Figure 4: The same as in Fig. 1 but for $\tan\beta = 10$ (upper window) and 50 (lower window). Also marked is the effect of imposing $\mu < 1\,\mathrm{TeV}$.

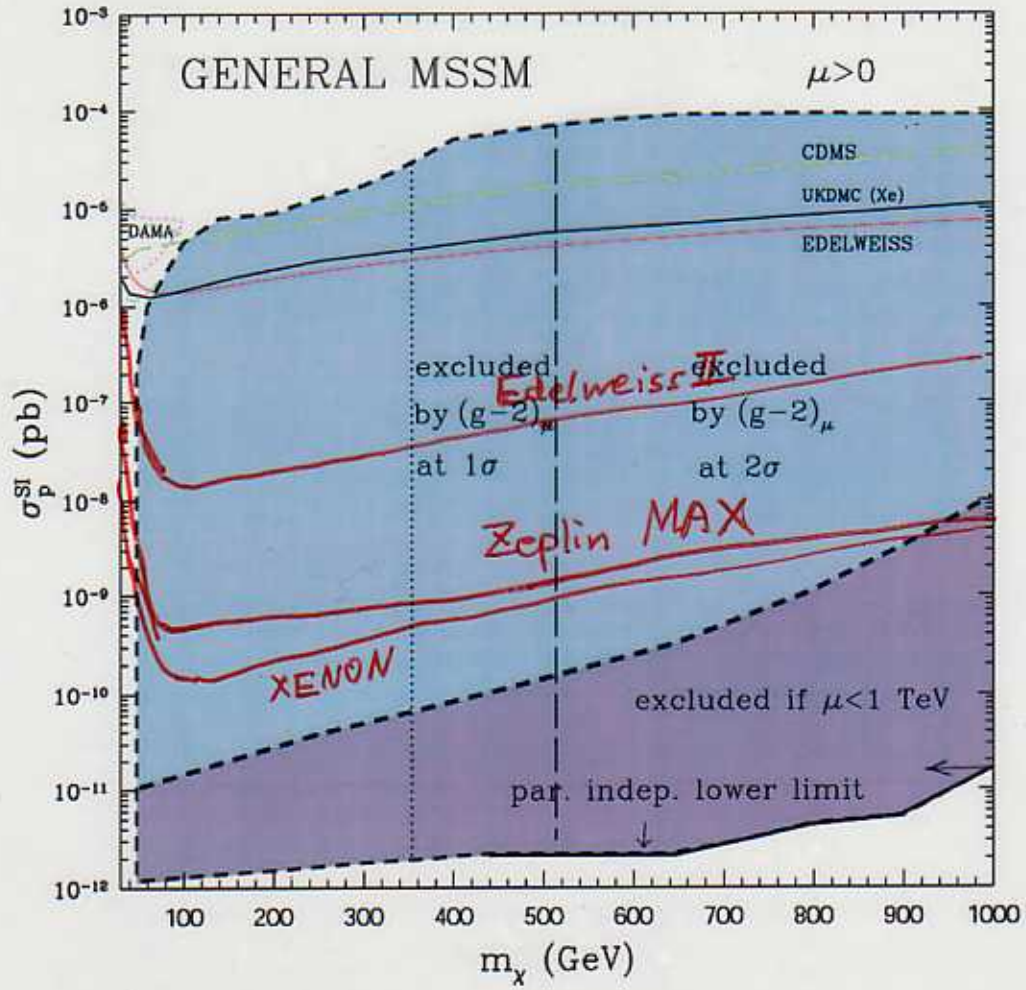

Figure 5: Ranges of $\sigma_p^{\rm SI}$ in the general MSSM *vs.* m_χ for $\mu > 0$, which are allowed by collider bounds, $b \to s\gamma$ and $0.1 < \Omega_\chi h^2 < 0.2$. Also marked are some results of recent experimental WIMP searches. The thick black line and a left–pointing arrow indicate a *parameter–independent* lower bound. The region below the dashed line is excluded if one imposes the constraint $\mu < 1\,\text{TeV}$. The ranges of m_χ to the vertical lines are excluded at $1\,\sigma$ and $2\,\sigma$ CL by the current discrepancy between the experimental value of $(g-2)_\mu$ and the Standard Model prediction.

$0 < m_{1/2} < 300$ GeV
$95 < m_0 < 1000$ GeV
$-3000 < A_0 < 3000$ GeV
$1.8 < \tan\beta < 25$

calculation of relic density performed by DarkSUSY. We have explicitly checked that there are no models in our data set which would be cosmologically allowed **only** if the stau coannihilations were included. We will also see later that expanding the upper bound on $m_{1/2}$ has serious consequences regarding the lower bound on the elastic scattering cross section. Also, the low value of $\tan\beta$ is set by the requirement that the top Yukawa coupling does not blow up before the GUT scale is reached.

Before we present the detailed analysis of cross section, a few remarks are in order. First, the $b \to s+\gamma$ constraint eliminates large portions of the $\mu < 0$ parameter space, in agreement with [27], [28]. Second, for both $\mu > 0$ and $\mu < 0$, we find no higgsino-like LSP models that are cosmologically important, in agreement with [28].

We plot the variation of the spin independent cross section versus the neutralino mass in Figure 2. Note that the complete allowed region is split into two parts by the annihilation channel into W^+W^-, which affects the relic density of neutralino. We consider two relic density constraints. Since the present observations favor the Hubble constant $h = 0.7 \pm 0.1$ and the total matter density $\Omega_M = 0.3 \pm 0.1$, of which baryons contribute $\Omega_b h^2 \approx 0.02$, we consider the range $0.052 < \Omega_\chi h^2 < 0.236$. However, we also examine effects of relaxing the relic density constraint to $0.025 < \Omega_\chi h^2 < 1$. The upper bound on $\sigma_{\chi-p}$ (of the theoretically allowed regions) comes from the lower bound on the relic density. The lower bound on M_χ comes from the existing constraints from the accelerator experiments. The upper bound on M_χ is a combination of the upper bound on relic density and of the bounds on the free parameters. The lower bound on $\sigma_{\chi-p}$ is not yet well understood, and it is the subject of this paper. Figure 2 also includes some recent and future direct detection experimental results [29, 30, 31, 32, 33]. Note that the parameter space defined by Eq. (6) corresponds to the region of $\sigma_{\chi-p}$ - M_χ plane bounded by the two closed solid lines. Therefore, $\sigma_{\chi-p} > 10^{-46}\text{cm}^2$ for these models, or equivalently, assuming a ^{73}Ge target, the dark matter density $\rho_D = 0.3\,\text{GeVc}^{-2}\text{cm}^{-3}$, the WIMP characteristic velocity $v_0 = 230\ \text{km s}^{-1}$ and following Ref. [34], the event rate $R > 0.1\ \text{ton}^{-1}\text{day}^{-1}$. Hence, the most ambitious future direct detection experiments may be able to explore a large portion, if not all, of the these models.

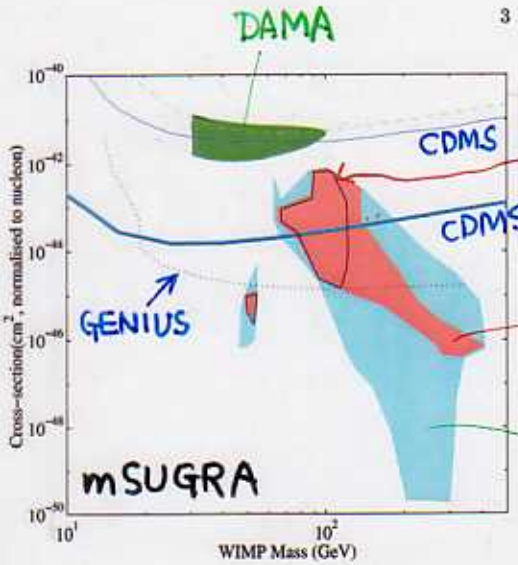

$0.052 < \Omega_\chi h^2 < 0.236$
$m_{1/2} < 300$GeV

$0.052 < \Omega_\chi h^2 < 0.236$
$m_{1/2} < 1$

$0.025 < \Omega_\chi h^2 < 1$
$m_{1/2} < 1$

FIG. 2: The cross section for spin-independent χ-proton scattering is shown. Current accelerator bounds, including $b \to s+\gamma$ are imposed through the DarkSUSY code. The top dark region is the DAMA allowed region at 3σ CL. The dashed curve is the DAMA 90% CL exclusion limit from 1996 (obtained using pulse-shape analysis). The thinner solid curve is the current CDMS 90% CL exclusion limit, the thicker solid curve is the projected exclusion limit for CDMS II experiment and the dotted curve is the projected exclusion limit for the GENIUS experiment. The light shaded regions denote mSUGRA models passing the $0.025 < \Omega h^2 < 1$ constraint and with the upper bound $m_{1/2} < 1$ TeV. As discussed in the text, this region shows that including stau coannihilations into the relic density calculation has a dramatic effect on the lower bound on $\sigma_{\chi-p}$ for $m_{1/2} > 300$ GeV ($M_\chi > 120$ GeV). Restricting the relic density further to $0.052 < \Omega h^2 < 0.236$ yields the darker regions within the lighter regions and restricting also the upper bound on $m_{1/2} < 300$ GeV (Eq. (6)) gives the regions bounded by the closed solid curves.

B. Results and Analysis

As mentioned above, the dominant contribution to spin independent elastic scattering is usually the Higgs boson exchange. Figure 3 illustrates this relationship within our results. The nearly perfect 45 degree line in the figure indicates good agreement between the total cross section as evaluated by DarkSUSY and the cross section calculated including the exchange of Higgs bosons only (in the approximation explained below). We will, therefore, concentrate on the Higgs boson exchange and will postpone the discussion of squark exchange to the end of this section.

The contribution of Higgs boson exchange can be found in the literature [4, 10, 13, 15, 35, 36, 37]. It is of the following form:

$$\sigma_{h,H} \sim |(f_u + f_c + f_t)A^u + (f_d + f_s + f_b)A^d|^2, \quad (7)$$

where $f_u \approx 0.023, f_d \approx 0.034, f_s \approx 0.14, f_c = f_t = f_b \approx 0.0595$ parametrize the quark-nucleon matrix elements and

$$A^u = \frac{g_2^2}{4M_W}\left(\frac{F_h}{m_h^2}\frac{\cos\alpha_H}{\sin\beta} + \frac{F_H}{m_H^2}\frac{\sin\alpha_H}{\sin\beta}\right), \quad (8)$$

$$A^d = \frac{g_2^2}{4M_W}\left(-\frac{F_h}{m_h^2}\frac{\sin\alpha_H}{\cos\beta} + \frac{F_H}{m_H^2}\frac{\cos\alpha_H}{\cos\beta}\right), \quad (9)$$

(cf) WMAP
$0.094 < \Omega h^2 < 0.129$ (1σ)
$0.076 < \Omega h^2 < 0.145$ (2σ)

IV. Summary

■ Accurate calculation of $\Omega_\chi h^2$ in the MSSM

with full cross section σ
exact thermal average $\langle \sigma v \rangle$
accurate treatment of Boltzmann eq.
coannihilation

WMAP: $\Omega_\chi h^2 = 0.1126^{+0.016}_{-0.018}$

$\longrightarrow$ Constrained MSSM (CMSSM) is

strongly constrained by WMAP.

Allowed "line" in the $(m_0, m_{1/2})$ plane

■ Direct detection rate

Parameter independent lower limits in the MSSM

Spin–independent $\chi p \to \chi p$ cross section

For $\mu > 0$ and $440\,\mathrm{GeV} \lesssim m_\chi \lesssim 1020\,\mathrm{GeV}$,

$\sigma_p^{\mathrm{SI}} \gtrsim 2 \times 10^{-12}\mathrm{pb}$.